UNIVERSITY OF WEST LONDON
The Career University

UWL REPOSITORY

repository.uwl.ac.uk

GPR analysis of clayey soil behaviour in unsaturated conditions for pavement engineering applications

Tosti, Fabio ORCID: https://orcid.org/0000-0003-0291-9937, Benedetto, Andrea, Bianchini Ciampoli, Luca, Lambot, Sébastien, Patriarca, Claudio and Slob, Evert (2016) GPR analysis of clayey soil behaviour in unsaturated conditions for pavement engineering applications. Near Surface Geophysics, 14 (2). pp. 127-144. ISSN 1873-0604

http://dx.doi.org/10.3997/1873-0604.2016011

This is the Accepted Version of the final output.

UWL repository link: https://repository.uwl.ac.uk/id/eprint/2191/

Alternative formats: If you require this document in an alternative format, please contact: open.research@uwl.ac.uk

Copyright:

Copyright and moral rights for the publications made accessible in the public portal are retained by the authors and/or other copyright owners and it is a condition of accessing publications that users recognise and abide by the legal requirements associated with these rights.

Take down policy: If you believe that this document breaches copyright, please contact us at open.research@uwl.ac.uk providing details, and we will remove access to the work immediately and investigate your claim.

GPR analysis of clayey soil behaviour in unsaturated conditions for pavement engineering and geoscience applications

Fabio Tosti[1,*], Andrea Benedetto[2], Luca Bianchini Ciampoli[2], Sébastien Lambot[3], Claudio Patriarca[4], Evert C. Slob[5]

[1]School of Computing and Engineering, University of West London (UWL), St Mary's Road, Ealing, W5 5RF, London, United Kingdom

[2]Department of Engineering, Roma Tre University, Via Vito Volterra 62, 00146, Rome, Italy; e-mail: fabio.tosti@uniroma3.it; andrea.benedetto@uniroma3; bianchini.ciampoli@gmail.com

[3]Earth and Life Institute, Environmental Sciences Université catholique de Louvain (UCL) Croix du Sud 2 box L7.05.02, 1348 Louvain-la-Neuve, Belgium; sebastien.lambot@uclouvain.be

[4]Statoil ASA, Sandsliveien 90, 5254 Sandsli, Norway; clpa@statoil.com

[5]Delft University of Technology, Faculty of Civil Engineering and Geosciences, Section of Applied Geophysics and Petrophysics Department of Geoscience & Engineering, Stevinweg 1, Delft 2628 CN, The Netherlands; e.c.slob@tudelft.nl

* Corresponding author: mail: fabio.tosti@uniroma3.it; tel: +39 0657333543

Abstract

Clay content is one of the primary cause of pavement damages, such as subgrade failures, cracks and pavement rutting, thereby playing a crucial role in road safety issues as an indirect cause of accidents. In this paper, several ground-penetrating radar (GPR) methods and analysis techniques were used to non-destructively investigate the electromagnetic behavior of sub-asphalt compacted clayey layers and subgrade soils in unsaturated conditions. Typical road materials employed for load-bearing layers construction, classified as A1, A2 and A3 by the American Association of State Highway and Transportation Officials (AASHTO) soil classification system, were used for the laboratory tests. Clay-free and clay-rich soil samples were manufactured and adequately compacted in electrically and hydraulically isolated formworks. The samples were tested at different moisture conditions from dry to saturated. Measurements were carried out for each water content using a vector network analyzer spanning the 1–3 GHz frequency range, and a pulsed radar system with ground-coupled antennas, 500 MHz center frequency. Different theoretically-based methods were used for data processing. Promising insights are shown to single out the influence of clay in load-bearing layers and subgrade soils, and its impacts on their electromagnetic response at variable moisture conditions.

List of keywords

clay detection; ground-penetrating radar; SFCW; soil moisture; road pavement; Rayleigh scattering; full-wave inversion, surface reflection method, volumetric mixing formulae

INTRODUCTION

Clay detection in soils is a key topic of research in many fields of application such as construction (Miqueleiz *et al.* 2012), pavement (Uzan 1998) and geotechnical engineering (Abusharar and Han 2011), agriculture (Robinson and Phillips 2001), and Earth sciences in general (Mahmoudzadeh *et al.* 2011). Overall, the interaction between water and clay plays a very important role in the health conditions of pavements due to the considerable swelling properties of clay (Wuddivira *et al.* 2012), since it is capable to exert significant effects on the stability of soils behavior under loading.

The chemical and mechanical behavior of clay, has been widely investigated in the past. As a rule of thumb, it is conventionally established to model the hydrodynamic behavior of plastic soils during wetting-drying cycles (Dudoignon *et al.* 2007). Richard *et al.* (2001) argued that particle arrangements along with their mineralogical nature can notably affect the properties of clayey soils under compressive or drying stress cycles. More recently, Beroya, Aydin, and Katzenbach 2009 have also proved that clay minerals abundance mainly governs the cyclic behavior of silt-clay mixtures.

Several procedures have been established over the years to limit the effects of clay in soils for construction and rehabilitation of transport infrastructures. In this regard, the use of geogrids (Abdi Sadrnejad, and Arjomand 2009) or additives (Pakbaz and Alipour 2012) are very common practices. When suitable strength and deformation properties of soils cannot be ensured by excessive abundances of plastic material, extra reinforcing steel to foundations and slabs as well as earthmoving operations for removing waste materials are instead usually carried out (Wood, Osborne, and Forde 1995). Among the most common destructive techniques for clay investigation, core sampling relies on an undeniable accuracy. However, coring is a local technique and it might not be representative of large areas; in addition to that, this method is invasive, expensive and time consuming.

The demand for non-destructive testing techniques (NDTs) in this field of application and beyond is increasing nowadays. To cite a few, acoustic methods like falling weight deflectometer (FWD) techniques (Benedetto *et al.* 2014a) are widely used to evaluate the strength and deformation properties of clayey soils, as well methods relying on spectral analyses, such as the vis-NIR spectroscopy (Viscarra Rossel *et al.* 2009), or infrared imaging (Srasra *et al.* 1994) of soil materials. However, most of the NDTs are not time-efficient, since they cannot be continuously implemented on roads, nor cost-effective for road inspection and maintenance. Amongst the main electromagnetic (EM) methods fit for purposes, advanced high-resolution radiometer (AVHRR) (Odeh and McBratney 2000) and electromagnetic induction (EMI) (Triantafilis and Lesch 2005) can be considered as other very effective techniques, although the scale domain of investigation or the long time required for surveying are not suitable for pavement engineering applications.

It is therefore clear how an effective high-performance method capable to provide large-scale reliable measurements with a high spatial resolution, is nowadays required. In line with this, ground-penetrating radar (GPR) has proved to be one of the most powerful diagnostic non-destructive tools that enables to collect data rapidly in the field (Saarenketo and Scullion 2000;Benedetto *et al.* 2012a; Tosti et al. 2014a). GPR is being increasingly employed in a range of many application areas such as planetary exploration, cultural heritage protection, Earth sciences, and engineering applications (Daniels 2004). This instrument allows to infer the physical conditions of subsurface relying on the transmission/reception of short EM impulses in a given frequency band (Van der Kruk and Slob 2004; Slob, Sato, and Olhoeft 2010;).

GPR was first used in traffic infrastructure surveys in 1970s by the Federal Highway Administration (FHWA) for testing in tunnel investigation (Morey 1998). The main applications in this field range from physical to geometrical inspections of pavement layers. They broadly include the evaluation of layer thicknesses (Al-Qadi and Lahouar 2004), the assessment of damage conditions in hot mix asphalt (HMA) layers (Scullion, Lau, and Chen 1994), load-bearing layers and subgrade soils (Saarenketo and Scullion 2000), the inspection of

concrete structures (Huston *et al.* 1999; Benedetto *et al.* 2012b). New frontiers on the use of GPR in pavement engineering have been also recently tackled on the possibility to infer mechanical properties of road pavements and materials from their EM characteristics (Benedetto and Tosti 2013; Tosti *et al.* 2014b). In addition, FDTD simulation-based approaches of the GPR signal have been implemented for analysing the GPR responses of typical scenarios of pavement faults (Benedetto *et al.* 2014b).

Many studies in the literature have been devoted towards the evaluation of water content (Robinson *et al.* 2008). Applications in this field can be broadly classified according to the type of pavement and construction material, whereby different radar systems and processing techniques can be specifically employed. Concerning subsurface moisture measurements in subgrade soils, GPR can bridge the gap between high-resolution data (from ~10^{-2} m to 10^{-1} m) by minor destructive techniques, such as capacitance probes (Wobshall 1978) and time domain reflectometry (TDR) (Fellner-Feldegg 1969), and low-resolution techniques (~10 m) by remote sensing investigations (Wagner *et al.* 2007), thereby ranking effectively as an intermediate-scale effective technology (from ~10^{-1} m to 1 m) (Lambot *et al.* 2006, Minet *et al.* 2011). Several approaches exist for determining the volumetric water content (VWC) θ by GPR (Huisman *et al.* 2003). An estimate of the relative dielectric permittivity ε_r is firstly carried out, and a petrophysical relationship is then used to convert ε_r into θ. Among such expressions, the empirical equation proposed by Topp, Davis, and Annan (1980) is undoubtedly the most used for this purpose. From a theoretical point of view, θ can be also related to ε_r by using volumetric mixing formulae, which use the volume fraction and the dielectric permittivity of each soil constituent to derive a relationship between them (Dobson *et al.* 1985, Roth *et al.* 1990).

Overall, the aforementioned methods for moisture evaluation rely on the estimates of the relative dielectric permittivity of soils, and the use of core sampling is mostly needed for calibrating the system. In this regard, research activities are increasingly being focused on the use of efficient and self-consistent techniques, namely, capable to minimize or avoid the use of

destructive samplings for calibration. Lambot *et al.* (2004a) evaluated the dielectric properties of unsaturated soils at the laboratory scale by relating the imaginary part of the dielectric permittivity and the frequency of investigation. Moreover, a Rayleigh scattering-based method has been used by Benedetto (2010) and Benedetto *et al.* (2015) for directly predicting the volumetric water content in soils, thereby enabling to avoid the use of any calibrations of the system.

The GPR-based detection of clay content has been mainly investigated over the years in studies applied at the field scale (Gómez-Ortiz *et al.* 2010, De Benedetto *et al.* 2012) and, partly, at the laboratory scale (Saarenketo 1998). More recently, advances in the research have registered several clay-dedicated laboratory studies specifically focused on achieving high-resolution estimates on different textured soil materials using several self-consistent processing techniques and different radar systems (Patriarca *et al.* 2013, Tosti *et al.* 2013).

METHODOLOGY AND OBJECTIVES

In this paper, it is analyzed the ability of GPR to detect clay in different types of soil at variable moisture contents by using several tools and signal processing techniques. Three types of soil classified by the American Association of State Highway and Transportation Officials (AASHTO 2011) as A1, A2, and A3 were used for laboratory testing. To single out the electromagnetic behavior of the above materials relative to clay presence, clay-free and clay-rich conditions amounting up to 15% by weight were manufactured. The consistency of results was validated through permittivity-based methods, namely, the full-wave inversion method, the surface reflection method, and the volumetric mixing formulae. In addition, a Rayleigh scattering-based method working in the frequency domain was employed for the analyses.

The possibility to detect clay in load-bearing layers and subgrade soils for preventing structural failures of pavements and restraining the risk of severe damage can be considered as the main task of this paper, as part of an important countermeasure in quality control, rehabilitation, and

maintenance operations made in transport infrastructures for improving transport safety conditions.

More specifically, the aforementioned processing techniques were applied on data collected from samples of compacted loose materials, representing conditions from load-bearing layers and subgrade soils, which were investigated using different GPR systems.

THEORETICAL BACKGROUND

Full-Wave Inversion Technique

The radar model

Lambot *et al.* (2004a) proposed an intrinsic far-field antenna model combined with planar layered media Green's functions where a local homogeneous field distribution is assumed for the backscattered field over the antenna aperture. Therefore, the antenna radiation properties can be described by an equivalent single electric dipole approximation. In such system, the wave propagation between the source point and the radar transmission line reference plane, as well as the antenna-medium interactions, can be described, on the basis of the linearity of Maxwell's equations, by means of complex, frequency-dependent global reflection and transmission coefficients. Equation (1) describes the relationship between the radar-measured field and the 3D layered medium Green's function in the frequency domain (Lambot *et al.* 2004a):

$$S_{11}(\omega) = \frac{b(\omega)}{a(\omega)} = R_i(\omega) + \frac{T(\omega) G_{xx}^{\uparrow}(\omega)}{1 - R_s(\omega) G_{xx}^{\uparrow}(\omega)} \quad (1)$$

with $S_{11}(\omega)$ representing the raw radar signal as the ratio between the backscattered field $b(\omega)$ and incident field $a(\omega)$ at the radar transmission line reference plane, and ω describing the angular frequency. $R_i(\omega)$ stands for the global reflection coefficient of the antenna in free space, while $\mathrm{T}(\omega) = T_i(\omega)\, T_s(\omega)$ with $T_i(\omega)$ being the global transmission coefficient for fields incident from the radar reference plane onto the source point, and $T_s(\omega)$ being the global transmission coefficient for fields incident from the field point onto the radar reference plane. $R_s(\omega)$ stands for the global reflection coefficient for the field incident from the layered medium

onto the field point, and $G_{xx}^{\uparrow}(\omega)$ is the layered medium Green's function. Such function is defined as the scattered *x*-directed field $E_x(\omega)$ at the field point for a unit-strength *x*-directed electric source $J_x(\omega)$ at the source point, and it can be theoretically written as (Slob and Fokkema 2002):

$$G_{xx}^{\uparrow}(\omega) = \frac{1}{4}\pi \int_0^{\infty} \tilde{G}_{xx}(k_p, \omega) dk_p \tag{2}$$

$$\tilde{G}_{xx}(k_p, \omega) = \left(\frac{\Gamma_n R_{TM}}{\eta_n} - \frac{\xi_n R_{TE}}{\Gamma_n}\right) \exp(-2\Gamma_n h_n) \tag{3}$$

where subscript TM and TE stand, respectively, for transverse magnetic mode and transverse electric mode. The *R* global reflection coefficients describe the reflected part of the wave in each mode. $\Gamma_n = \sqrt{k_p^2 + \xi_n \eta_n}$ is the vertical wave number, where subscript *n* represents the number of layers and it is equal to 1 in equation (3) (index of the top layer (free space)), $\eta_n = \sigma_n + j\omega\varepsilon_n$ and $\xi_n = j\omega\mu_n$. The global TM-mode and TE-mode reflection coefficients at the $n = 1 \ldots N$ interface are given by:

$$R^{TM} = \frac{r_{n+1}^{TM} + R_{n+1}^{TM} \exp(-2\Gamma_{n+1} h_{n+1})}{1 + r_n^{TE} + R_{n+1}^{TM} \exp(-2\Gamma_{n+1} h_{n+1})} \tag{4}$$

$$r^{TM} = \frac{\eta_{n+1}\Gamma_n - \eta_n \Gamma_{n+1}}{\eta_{n+1}\Gamma_n + \eta_n \Gamma_{n+1}} \tag{5}$$

$$R^{TE} = \frac{r_n^{TE} + R_{n+1}^{TE} \exp(-2\Gamma_{n+1} h_{n+1})}{1 + r_n^{TE} + R_{n+1}^{TE} \exp(-2\Gamma_{n+1} h_{n+1})} \tag{6}$$

$$r^{TE} = \frac{\mu_{n+1}\Gamma_n - \mu_n \Gamma_{n+1}}{\mu_{n+1}\Gamma_n + \mu_n \Gamma_{n+1}} \tag{7}$$

The antenna characteristic functions $R_i(\omega), R_s(\omega)$ and $\mathrm{T}(\omega)$ can be determined through a proper calibration of the antenna, involving the measurement of the raw radar signal $\mathrm{S}_{11}(\omega)$ for particular antenna-medium configurations, for which the value of the Green's function can be calculated (e.g., measurements with the antenna at different heights over a copper sheet). In

particular the $R_i(\omega)$ coefficient, *i.e.*, the global reflection of the antenna in free space, can be derived by performing a radar measurement with the antenna pointed toward the sky. It is worth noting that once the antenna factors are determined, they can be considered as constant regardless from the type of medium investigated. Accordingly, all the antenna effects can be filtered out from the raw radar data in order to retrieve the value of the Green's function $G_{xx}^{\uparrow}(\omega)$.

Model inversion

This method relies on a comparison between the value of the Green's function measured on the test samples $G_{xx,mea}^{\uparrow}(\omega)$ and the value of a theoretically modeled Green's function $G_{xx,mod}^{\uparrow}(\omega)$, retrieved through the aforementioned theoretical assumptions.

It is therefore possible to model the behavior of the Green's function depending on fixed electromagnetic and geometrical parameters, such as the relative dielectric permittivity ε_n, the electrical conductivity σ_n, the wave number k_p, the number of layers *N* illuminated by the EM wave, the thickness h_n of the n^{th} layer, and the distance h_0 from the antenna phase centre to the surface of the investigated medium. A mono-layered configuration as well as a fixed distance of 0.32 m between the soil sample surface and the antenna aperture are considered in this study, with the equivalent point source in turn being located at 0.07 m from the antenna aperture.

It is then possible to build a field of dielectric parameter values, sized [*P*×*M*], with *P* and *M* being, respectively, the dimensions of the dielectric permittivity and the electrical conductivity vectors taken into account. Accordingly, a 3D matrix of Green's function $G_{xx,mod}^{\uparrow}(\omega)$ values can be produced in the evaluated frequency range, with dimensions [*P*×*M*×*F*], where $F = B/f_s$ is the number of collected frequencies, being *B* and f_s, respectively, the selected frequency bandwidth and the frequency step.

The inversion process consists in retrieving the dielectric parameters ε_n and σ_n of the analyzed materials starting from the measured radar data, expressed in terms of $G^{\uparrow}_{xx,mea}(\omega)$ rather than $S_{11}(\omega)$, and from the theoretically expected behavior of the modeled Green's function $G^{\uparrow}_{xx,mod}(\omega)$. These two unknown values are returned through a search for the best matching between measured and modeled Green's functions. In this regard, by defining a vector $\mathbf{b} = [\sigma_n, \varepsilon_n]$, the wanted value of $\mathbf{b}$ is the one minimizing an objective function $\varphi(\mathbf{b})$ expressing the error between measured and modeled Green's functions. In this study, the objective function is computed as follows (Patriarca et al. 2011):

$$\varphi(\mathbf{b}) = \sqrt{\frac{\sum_{f\,min}^{f\,max} |G_{xx,mea} - G^{(b)}_{xx,mod}|^2}{\sum_{f\,min}^{f\,max} |G_{xx,mea}|^2}} \tag{8}$$

Frequency dependence of conductivity

In the GPR frequency range, a frequency-dependent behavior of the material apparent conductivity (including dielectric losses) usually occurs. This is mainly due to relaxation mechanisms and Maxwell-Wagner effects in the soils. In this regard, it is worth mentioning the locally linear relationship between σ and f proposed by Lambot *et al.* (2004a):

$$\sigma(f) = \sigma_{f_i} + a(f - f_i) \tag{9}$$

where σ_{f_i} is the reference value of conductivity at the starting frequency f_i, which can be evaluated through the inversion process, and a is the variation rate of the $\sigma(f)$. Therefore, when considering σ_{n,f_i}, namely, the relevant conductivity for the n^{th} layer, variable in the range [10^{-1} ÷

10^{-4} Sm^{-1}], the parameters affecting the objective function must be taken into account in a new vector $\mathbf{b} = [\sigma_{n_{fi}},\ a,\ \varepsilon_n]$. Typical values of a lie in the range [$10^{-10} \div 10^{-12}$ Ssm^{-1}]. In this work, a constant value of a equals to 1×10^{-10} Ssm^{-1} is adopted, so that the sizes of vector **b** are related only with two dielectrics. It is worth mentioning how Lambot et al. (2004a) have found the linear relationship of Equation (9) to be very suited for the 1 – 2 GHz frequency range, while higher discrepancies of this model were observed for wider frequency intervals.

Implementing the Full-Wave Inversion method with the Time Domain Signal Picking approach

This approach has been adopted according to the results from Tosti *et al.* (2013), wherein laboratory tests were carried out on soil samples with same dimensions than those used in this work. In particular, a good effectiveness was proved in forecasting dielectric permittivity values by estimating the two-way travel time of the measured radar signal within the medium, being such estimates comparable to those coming from the application of Full-Wave Inversion (FWI) technique.

The method provides the application of an Inverse Fast Fourier Transform (IFFT) to convert the domain of the signal measured from spectral into time. Once having the transformed signal $g^{\uparrow}_{xx,mea}(t)$, the time delay Δt_1 between the air-medium and the medium-perfect electric conductor (PEC) reflections can be measured, by knowledge of the thickness h_1 of the formworks, and the wave velocity through the medium v_1 estimated by $v_1 = 2h_1/\Delta t_1$. It is therefore possible to retrieve the value of permittivity by letting $\varepsilon_{TDSP} = (c/v_1)^2$, where c is the speed of light in free space. From now on, such approach will be referred to as the Time Domain Signal Picking (TDSP) technique. Figure 1 shows a typical scenario of measured signal where the two aforementioned peaks of reflection are clearly identified.

FIGURE 1. Measured Green's function in the time domain $g^{\uparrow}_{xx,mea}(t)$ and time delay Δt_1 between air-medium and medium-PEC interfaces.

The implementation of the TDSP technique within a FWI approach subsequently provides to retrieve a first approximation value of dielectric permittivity ε_{TDSP} for each sample. As represented in the flowchart of Figure 2, this value can therefore be used as a starting point for a deeper analysis in the spectral domain, to be further refined for retrieving information about the other electromagnetic properties. The conventional FWI approach is then employed over a significant range of dielectric permittivity values, in the neighborhood of the value retrieved by the TDSP approach, namely, within the range ± 10% of the ε_{TDSP} value.

FIGURE 2. Flowchart representing the implementation of the TDSP technique within a FWI approach.

Surface Reflection Method

The use of the Surface Reflection Method (SRM) leads to the evaluation of the relative dielectric permittivity of a mono-layered system by comparing the amplitude of the air-soil interface reflection and the amplitude from the air- PEC interface, taken as a reference. Such approach is commonly employed when measuring with high-frequency off-ground GPR systems. (Davis and Annan 2002, Serbin and Or 2004).

When considering one soil characterized by a certain value of permittivity ε_r, the reflection coefficient *R* at the surface separating air and soil layers can be determined as follows (Redman *et al.* 2002):

$$R = \frac{1-\sqrt{\varepsilon_r}}{1+\sqrt{\varepsilon_r}} \tag{10}$$

where 1 is the value of the dielectric permittivity of the air. Equation (10) relies on the twofold assumptions of *i)* a negligible conductivity and *ii)* a simplified scenario of air layer over a homogeneous half space (Lambot *et al.* 2006). By considering that the magnitude of the reflection coefficient *R* at a given height position *h* above the surface can be also expressed as the ratio between the amplitude A_r of the reflection from the ground surface to the amplitude A_m of the reflection over a copper shield or a metal plate (with a reflection coefficient of -1), both measured at the same height *h* from the ground, it is possible to calculate the permittivity of the soil as:

$$\varepsilon_r = \left(\frac{1+\frac{A_r}{A_m}}{1-\frac{A_r}{A_m}} \right)^2 \tag{11}$$

This approach has the main advantage of providing an estimation of the soil permittivity without knowing the subsurface reflector position or the wave propagation velocity through the medium, as in case of TDSP applications. Nevertheless, it is clear how an inhomogeneous water distribution within the medium could lead to different results depending on the method applied. Indeed, for higher particle-sized materials, a gravimetric behavior is prevalent for the water, which tends to stratify at the bottom as a water table. This water content clearly influences results of FWI or TDSP methods, while it could be neglected by SRM if the water table is too deep with respect to the air-soil interface. Many literature studies have dealt with the capability of the SRM to sense water content on the basis of soil physical properties. Huisman *et al.* (2003) considered such influence as relevant up to depths of 20 cm. Conversely, Serbin and Or (2004) narrowed the reliability of this method to the first 1 cm below the soil surface. Therefore, it seems clear how this uncertainty can be considered as the main drawback of the SRM (Lambot *et al.* 2004b). Further drawbacks include a high dependence of this technique on surface roughness, along with a high sensitivity to moisture for lower water contents (Davis *et al.* 1994). On the other hand, it is also worth citing the remarkable advantage of a significant lightness in computational requirements.

Volumetric Mixing Formulae

Volumetric Mixing Formulae (VMF) rely on the volumetric fraction and the dielectric permittivity of each component of a multi-phase medium, and enable to assess the volumetric water content θ (Dobson *et al.* 1985, Roth *et al.* 1990).

By considering a medium with *n*-phases, the general expression of a VMF can be written as follows:

$$\varepsilon_r^\alpha = \sum_{i=1}^{n} f_i \varepsilon_{r,i}^\alpha \tag{12}$$

where α represents a geometrical fitting parameter depending on the inner structure of the medium (Lichtenecker and Rother 1931), while f_i and $\varepsilon_{r,i}^\alpha$ stand, respectively, for the volume fraction and the dielectric permittivity of the i^{th} component. By implementing Equation (12) on a three-phase system and by knowledge of the porosity ζ of the soil material, it is therefore possible to determine the permittivity of the medium:

$$\varepsilon_r = \left(\theta \varepsilon_w^\alpha + (1-\zeta)\varepsilon_s^\alpha + (\zeta-\theta)\varepsilon_a^\alpha\right)^{1/\alpha} \tag{13}$$

where ε_w^α, ε_s^α and ε_a^α are, respectively, the permittivity of free water, of the solid matrix and of the gaseous phase, and θ stands for the volumetric water content of the multi-phase system. According to this, the permittivity of the solid matrix can be evaluated by considering the relative permittivity of the multi-phase medium in dry conditions ε_r^{dry} $(\theta = 0)$, as follows (Patriarca *et al.* 2013):

$$\varepsilon_s = \left[\frac{\left(\varepsilon_r^{dry}\right)^\alpha - \zeta}{1-\zeta}\right]^{1/\alpha} \tag{14}$$

In case of clayey soils, it is necessary to consider a four-phase medium and, accordingly, a VMF expressed as follows (Roth *et al.*1990):

$$\varepsilon_r = \left(\theta \varepsilon_w^\alpha + (1-\zeta-f_c)\varepsilon_s^\alpha + (\zeta-\theta_v)\varepsilon_a^\alpha + f_c\varepsilon_c^\alpha\right)^{1/\alpha} \tag{15}$$

where f_c and ε_c^α stand for the volumetric content and the permittivity of the clay fraction, respectively. In addition, the permittivity of the soil matrix can be determined by considering the dry conditions of the system (Patriarca *et al.* 2013):

$$\varepsilon_s = \left[\frac{\left(\varepsilon_r^{dry}\right)^{\alpha} - \zeta - f_c \varepsilon_c^{\alpha}}{1-\zeta-f_c}\right]^{1/\alpha} \quad (16)$$

In this paper, values of ε_r^{dry} were retrieved from the work of Tosti *et al.* 2013, wherein laboratory tests on the same materials were carried out in dry conditions. Many efforts were devoted in the past to characterize the value of α, which can vary between -1 and 1. By letting $\alpha = 0.5$, it is assumed to have a wave travel time through the medium equal to the travel times within each singular component weighted by the volume (Birchak *et al.* 1974, Dobson *et al.* 1985, Gorriti and Slob 2005). Roth *et al.* (1990) proposed a value of α equals to 0.46 for a three-phase medium, while Dobson *et al.* (1985) retrieved a value of 0.65 for a four-phase mixture. An interesting work has been recently developed by Patriarca *et al.* (2013), who developed a method for determining the optimal α value for different clay-rich mixtures. In this work, a value of 0.5 is adopted for the α factor.

Among the main drawbacks of this method, it can be mentioned the need to have an a-priori knowledge of some physical properties of the multi-phase medium, as well as of the dielectric permittivity of each component.

Rayleigh Scattering Method

A recent approach relying on signal processing in the frequency domain was proposed by Benedetto (2010). The main advantage of the Rayleigh Scattering Method (RSM) consists in avoiding core sampling to calibrate the system, since the volume fractions of the three phases in the medium are not accounted for. In this regard, θ can be directly estimated by frequency analyses of the GPR signal without estimating the dielectric permittivity. The main assumption are that in the unsaturated domain, electromagnetic waves are scattered by water droplets (Drude 1902), thereby a shifting of the central frequency of the waves occurs (Bohren and Huffman 1983).

Rayleigh scattering is traditionally used to explain the shifting of the frequency of the scattered signals. A shift in the frequency distribution of the reflected signals has already been observed in the past; however, the cause of such shift was not identified or deeply investigated (Narayana and Ophir 1983; Ho, Gader, and Wilson 2004).

Overall, it is well-known that scattering is generated by singularities or non-homogeneities in electromagnetic impedance. The process can be described as Rayleigh scattering whether the dimensions of these non-uniformities are much smaller than the wavelength of the EM wave. Analytically, the size of a scattering particle is defined by the ratio $x = 2\pi r / \lambda$, where r is the radius of the particle, and λ represents the wavelength of the signal. According to this, Rayleigh scattering occurs in the small size parameter regime when $x \ll 1$. Scattering from larger spherical particles was explained by Mie (1908) for an arbitrary size parameter x. When small values of x are considered, the Mie theory falls in the Rayleigh approximation.

By means of both several assumptions on the three-phase porous medium properties and simplifications of the physics, Benedetto (2010) defined the following formulation:

$$I(\theta_s, f) = I_0(f)\frac{1+\cos^2\theta_s}{2R^2}\left[\frac{2\pi f}{c_0}\sqrt{\mu_r\left(\varepsilon_\infty + \frac{\Delta\varepsilon}{1+f^2\tau^2}\right)}\right]^4\left[\frac{\mu_r\left(\varepsilon_\infty + \frac{\Delta\varepsilon}{1+f^2\tau^2}\right)-1}{\mu_r\left(\varepsilon_\infty + \frac{\Delta\varepsilon}{1+f^2\tau^2}\right)+2}\right]^2\left(\frac{d}{2}\right)^6 \quad (17)$$

whit R being the distance between the observer and the particle, θ_s represents the angle of scattering, f is the frequency of the electromagnetic signal, c_0 is the velocity of free space, μ_r is the magnetic permeability, ε_∞ is the dielectric constant of the full-polarized medium at an infinite frequency electromagnetic field, $\Delta\varepsilon = \varepsilon_{static} - \varepsilon_\infty$ is the difference between the permittivity values of, respectively, a steady and an infinite frequency electromagnetic field, τ is the relaxation time, and d stands for the diameter of the particle. According to the water content, a non-linear modulation of the electromagnetic signal is produced by scattering. In this regard, the author demonstrated how the peak of frequency was a comprehensive indicator, negatively related to moisture. Accordingly, since scattering is caused by water presence in the medium, more scattering events are expected as the water content increases.

In line with Equation (17), it was observed how the several frequency components of the frequency spectra were differently scattered, depending on the soil type and water contents, with the peak of the frequency spectrum f_P being the frequency component having the maximum scattered intensity of the EM wave. On the basis of several experimental evidences, it was proposed the following regression law for determining water content θ, expressed in %, from the value of the peak of frequency f_P, expressed in Hz×10^8:

$$\theta = (A - f_P)/B \tag{18}$$

where A and B are regression parameters calibrated by means of laboratory tests on different soil samples. In this paper, the RSM was applied to analyse the behavior of clay-free and clay-rich soil samples and to provide further insights about water content evaluation in the soil types taken into account herein, according to Equation (18).

EXPERIMENTAL FRAMEWORK

Experimental design

The main purpose of the experimental design has been to provide a research scenario capable to sufficiently represent the electromagnetic behavior of clayey soils, outlined by the combination of different-textured soil samples in both clay-free and clay-rich conditions along with water contents from dry to saturation. A detailed description of the samples preparation protocols followed in this work, including compaction procedures and clay mixing, can be found in Tosti *et al.* 2013. In addition, standard procedures for cross-checking the homogeneous wet conditions within the soil samples have been implemented herein, as described later.

Test devices and equipment

Experimental tests were carried out using two different GPR systems. An ultra wideband (UWB) stepped frequency continuous wave (SFCW) radar, was set-up by using a vector network analyzer (VNA) manufactured by Hewlett Packard (8753C, 300 kHz – 3 GHz) to

collect data in the frequency domain (Figure 3a). More information on the antenna properties, the calibration procedures, the experimental setup for such type of off-ground measurements, as well as about the dimensions of the test formworks can be found in Tosti *et al.* 2013.

In addition, a pulsed radar system with ground-coupled antennas (pulseEKKO PRO manufactured by Sensors & Software Inc., Canada), 500 MHz center frequency of investigation, was used in a bi-static configuration and common offset (Figure 3b). Data were collected in the time domain, using a 40ns time window and a time step of 5×10^{-2} ns.

FIGURE 3. Test devices and equipment a) SFCW radar set-up using a vector network analyzer HP 8573C (Hewlett Packard Company, USA) and a linear polarized double-ridged broadband TEM horn BBHA 9120 A (Schwarzbeck Mess-Elektronik, Germany), in a mono-static configuration. b) PulseEKKO PRO 500 pulsed radar system, manufactured by Sensors & Software Inc., Canada.

Materials and laboratory testing

Typical road materials used for unbound pavement layers construction and subgrade soils were used for laboratory testing. In more details, three different soil types, classified by the AASHTO soil classification system as A1, A2, and A3 were considered, being, respectively, gravel (A1, grain size 4-8 mm), coarse sand (A2, grain size 1-2 mm), and fine sand (A3, grain size 0.125-0.250 mm).

Concerning the clay-rich samples, an amount of 15% by weight of bentonite clay was added within the above three types of undisturbed materials. The Colclay A90 bentonite clay, manufactured by Ankerpoort NV, The Netherlands, is mineralogically mainly composed by smectite, consisting of silica (62% by weight) and alumina (21% by weight) sheet-like bounded particles. Mineral thin units get separated by water intrusion between the particles, thereby causing a sudden dispersion of the bentonite in the water.

Increasing amounts of water were gradually added to the soil samples from dry up to saturated conditions. After the mixing and compaction procedures, the bulk density of each soil sample was collected. To ensure homogeneous moisture conditions within the samples, a number of three samplings was carried out in the barycenter and in the lower and upper corners of each sample, alongside the diagonal line of the specimens, such that it was possible to determine the average volumetric water content of each sample after drying in the oven the sampled material. A relatively high moisture homogeneity was broadly verified in all the samples according to the low values of standard deviation determined between the aforementioned three sampled amounts of VWC (i.e., standard deviation σ_θ < 2%). A thorough list of the main physical properties of the dry-member materials used in this work, including bentonite clay, can be found in Tosti *et al.* 2013.

RESULTS AND DISCUSSION

Soil behavior analysis through permittivity-based methods

According to the flowchart of Figure 2, permittivity values ε_{TDSP} from the TDSP technique were firstly estimated from the measured signal in time domain, after implementing the IFFT of the responses measured in the frequency domain.

In a second step, the inversion process is run. According to this, each measured signal $G^{\uparrow}_{xx,mea}(\omega)$ is compared with a 3D matrix of Green's functions $G^{\uparrow}_{xx,mod}(\omega)$, sized [$P$×$M$×$F$], being P = 75 (i.e., ε_n), M = 60 (i.e., σ_n), and F = 640 (i.e., number of frequencies collected), being n = 1, with a relatively large parameter space used for running such inversions. As previously mentioned, the target value of ε_n can be searched in the parameter space defined by ± 10% of the ε_{TDSP} value of first approximation. Furthermore, the frequency-dependent electrical conductivity $\sigma(f)$ has been evaluated according to Equation (9), being the parameter space for σ_{f_i} variable in the range [10^{-1}÷10^{-4} Sm^{-1}] within a bandwidth B spanning the 1 – 3 GHz

frequency range. Finally, the *F* parameter has been obtained by the ratio between the above cited bandwidth *B* and a frequency step f_s of 3.125 MHz.

Figure 4a,b depicts two examples of measured and modeled responses in the frequency and time domain by FWI application.

FIGURE 4. Measured and modeled Green's functions in the frequency (amplitude $|G_{xx}^{\uparrow}|$ and phase $\angle G_{xx}^{\uparrow}$) and time ($g_{xx}^{\uparrow}$) domain. (a) soil sample 23 (A3, clay = 0%, θ = 10.9%); (b) soil sample 45 (A3, clay = 15%, θ = 9.7%).

As it can be seen in the $|G_{xx}^{\uparrow}|$ plots, a smoother behavior can be observed in case of clay presence (Figure 4b), being the same soil type (i.e., A3) considered in both figures, with comparable volumetric water contents. Amplitudes for the clay-free A3 soil sample (Figure 4a) reach higher peak values than in the presence of clay. Concerning the Green's functions in the $g_{xx}^{\uparrow}$ time domain, two main peaks of reflection can be clearly singled out in both these figures. It is also worth noticing how signal amplitudes in the time domain can be affected by mismatches occurring in the frequency domain. The comparison between the two $g_{xx}^{\uparrow}$ plots of Figure 4a,b for the clay-free and the clay-rich soil samples shows the positions of the first main peaks of reflection (namely, the air-soil interfaces at the subsequent zero-amplitude positions along the *x* axis) at 2.03 ns and 2.02 ns, respectively. Coherently, the second main peaks of reflection (namely, the soil/PEC interfaces at the subsequent zero-amplitude positions along the *x* axis) are measured at 3.63 ns and 3.43 ns, thereby providing time distances Δt = 1.60 ns for (a) and Δt = 1.40 ns for (b). Such trend can be considered a comprehensive case study for the overall behavior of the road materials investigated, being the position of the first main peak of reflection approximately the same for all the samples, while the second main position usually locates in floating time distances, as expected by the different physical conditions manufactured in the specimens. Relatively good matches between permittivity estimates with TDSP and FWI

techniques have been found, whereby errors ≤ 8%, 7%, and 6% can be detected for A1, A2, and A3 soil types, respectively.

In addition to the above two techniques for permittivity estimation, the SRM was used to retrieve further values of dielectric permittivity ε_{SRM} from the measured signals in the time domain representing each soil sample. On the other hand, permittivity values ε_{VMF} from the VMF approach were also inferred by exploiting the physical properties of the soil samples along with the water contents gravimetrically determined.

Methods comparison

Table 1 lists the values of relative dielectric permittivity assessed by the above four methods in both clay-free and clay-rich conditions. The overall trend proves how increasing values of relative dielectric permittivity are reached for higher water amounts in samples. Moreover, considerably lower values of permittivity can be observed in clayey samples, probably due to the swelling properties of clay that tightly bound water particles by molecular forces preventing a full polarization of the water dipoles when the EM field is applied. Much more than in the case of clay-free samples, the four methods return similar permittivity values for the clay-rich samples, whereby slighter variations of permittivity between dry-member and end-member (i.e., saturated) cases are also encountered. Considerable differences of dielectrics among all the four approaches are instead detected in clay-free cases.

TABLE 1. Relative dielectric permittivity values retrieved using different processing methods for 0% and 15% clay samples.

The plots in Figure 5a-f provide interesting insights on the EM response of different textured soils with varying clay and water contents. Petrophysical relationships from Topp, Davis, and Annan (1980) were used here for best comparing the performances of the processing techniques employed with the empirical estimates of relative dielectric permittivity based on the water

content measurements. Both the Topp's general expression and the Topp's site-specific relationship for the Rubicon sandy loam (SL) soil type, with grain size distribution comparable to the soil types analyzed herein and very low clay contents, were taken into account for the analyses on the clay-free soil samples, while only the Topp's general expression was considered for the clay-rich member cases.

Concerning clay-free samples behavior (i.e., Figures 5a-c), it can be argued how the agreement of the processing methods in θ estimate is highly dependent on the soil texture. In particular, the lower is the grain size of the material, the similar and closer are the EM responses retrieved. To broadly quantify the errors between permittivity estimates by different approaches, the Normalized Root Mean Square Deviation (NRMSD) index has been therefore evaluated for each pair combination of methods, as follows:

$$NRMSD = \frac{\sqrt{\frac{\sum_{i=1}^{n}(\varepsilon_{r_i}^{*}-\varepsilon_{r_i})^2}{n}}}{\varepsilon_{r_{max}}-\varepsilon_{r_{min}}} \tag{19}$$

where $\varepsilon_{r_i}^{*}$ and ε_{r_i} are the i^{th} estimated permittivity values for, respectively, the considered and the reference method, n is the number of parameters, $\varepsilon_{r_{max}}$ and $\varepsilon_{r_{min}}$ are, respectively, the maximum and minimum permittivity values within the population of the reference method taken into account. Table 2 lists the NRMSD values for the whole set of processing techniques that have been compared each other. Such statistics confirm a good reliability in permittivity estimates of the A3 soil type, with negligible errors. On the contrary, these errors increase for higher grain sizes up to 0.84 (i.e., NRMSD value by FWI and Topp (general) comparison for A1 soil samples).

TABLE 2. Normalized Root Mean Square Deviation (NRMSD) values in clay-free soil samples by comparing the different permittivity-based methods.

Experimental tests have highlighted that the greater the grain size of samples, the more remarkable the heterogeneities observed in water distribution. In case of the A1 soil type already with relatively low moisture contents, the experimental observations have shown how a free-water layer had begun to form at the bottom of the test box. This could be due to a very low threshold of loosely bound molecular and capillary water, being the amount of capillary water controlled by the soil texture, soil structure, organic matter and gravity (Lyon and Buckman 1937). Accordingly, capillarity tends to have a greater contribution in finer-textured materials, and much more capillary meniscus around single or multiple particles are formed. This can be singled out according to the trend of permittivity values retrieved by the FWI with respect to SRM, VMF, and Topp-based relationships. When considering A1 soil samples (Figure 5a) in the gravel size domain, capillarity occurs up to very low volumetric water contents. Indeed, similar estimates can be seen up to θ = 2.68%, beyond which the FWI begins to return very much higher values of permittivity than the other techniques. Useful insights about the hydraulic and EM behaviors of similar gravel aggregates for increasing water contents can be found in Scullion and Saarenketo (1997).

One main explanation for this behavior lies on the own theoretical principles of these processing techniques. By experimental evidence, the SRM approach returns relatively flat values of permittivity within the A1 and A2 soil samples, respectively in Figures 5a and 5b, with an increasing trend observed for the last two member-cases of A2 soil samples when the permittivity approaches the analogous estimates by the other processing methods. In line with this, a more regular and slight increasing behavior can be also seen in A3 soil samples (Figure 5c), wherein major effects of capillarity occur. Within this framework, when water content increases in coarser-sized materials such as A1 soils, the upper unsaturated volume of the formwork retains the same levels of loosely bound water, while the thickness of the water layer progressively increases at the bottom. Since the SRM strongly relies on surface reflections, the higher is the grain size of the soil (i.e., lower amounts of loosely bound and capillary water), the more different will be the values of permittivity retrieved with respect to the other processing

techniques considered herein. Such behavior diverts when the depth to water layer approaches the surface, namely, for moisture conditions close to saturation, and the SRM approach becomes more sensitive to free water, thereby returning higher dielectrics. Where loosely bound water contribution and capillary effects are higher (i.e., finer-textured soils), the SRM returns permittivity values more consistent with the water added to the samples (i.e., A3 soil in Figure 5c).

A certain weak sensitivity to water is instead observed for permittivity estimates using the VMF method, which slightly rise for finer-textured materials. Relying on the theoretical assumptions of a homogeneous distribution of the multi-phase soil components within each weighted volume and same wave propagation velocity through the medium, the relevant permittivity estimates do not reflect the real distribution of water within the formwork. Such behavior is more emphasized in coarser materials, such as the A1 soil sample, than in A2 and A3 soils, where capillarity effects contribute at more homogeneously distributing moisture within the multi-phase volume of the specimen.

The FWI approach takes instead into account the whole thickness of the samples, and returns a modeled signal which includes all the possible information of the wave related to a non-homogeneous distribution of water within the depth domain investigated.

On the other hand, the EM behavior in clay-rich soil samples (i.e., Figures 5d-f) is strongly related to the presence and amount of clay particles, which deeply affect how the water molecules adhere to the particle surface. In more details, the water dipole is oriented according to the electrical charge of the clay particle when applying an EM field, by virtue of molecular forces (Benedetto 2010). In this case, a high-density layer of tightly bound water around the particle surface is formed. When water content increases, a ticker film of oriented dipoles creates, and the outer water changes into the so-called loosely bound layer, since the bonding forces decrease with the distance from the mineral surface. Basically, the aforementioned layers of adsorbed water consist of monomolecular layers which surround negatively charged mineral surfaces and further absorption water layers that can be tightly or loosely bound (Mitchell

1992). In this regard, when clay particles are present and water molecules are bound in the form of adsorbed water, the EM field applied by GPR enables to orientate only the loosely bound water dipoles. When increasing moisture contents, a ticker film of water around the soil particles occur, thereby enabling the polarization of the outer dipoles. This reflects in a lower variability of the soil dielectric properties with water content, regardless of the amount of θ.

A very good consistency in permittivity estimates is observed by the application of the FWI and SRM methods within all the types of soil investigated, being the NRMSD indexes equal to 0.12, 0.16 and 0.21 for, respectively, A1, A2 and A3 soil samples (Table 3). This is due to fairly homogeneous water content conditions throughout the whole thickness of the formwork, such that lower differences between near surface permittivity values by SRM and full-depth dielectrics by FWI occur. In addition to this, it is worthwhile to note how the application of the VMF approach mostly overestimates the ε_{VMF}values (i.e., A2 and A3 soils in Figures 5e and 5f), since the water content contribution is completely taken into account by the theoretical model, while the electrical losses due to the rates of tightly bound water to clay particles are not considered.

Overall, the application of the Topp's general relationship returns higher values of dielectric permittivity for all the three types of soil. The VMF approach provides in turn intermediate permittivity estimates between the Topp's approach and the FWI and SRM techniques. Finally, it should be noted how the best agreement among the various approaches is verified for the A1 soil type (Figure 5d).

FIGURE 5. Plots of volumetric water contents θ vs dielectric permittivity values ε_r by different permittivity-based methods in clay-free – A1 (a), A2 (b), A3 (c) – and 15% of clay conditions – A1 (d), A2 (e), A3(f) –.

TABLE 3. Normalized Root Mean Square Deviation (NRMSD) values in clay-rich soil samples (15% of clay) by comparing the different permittivity-based methods.

Soil behavior analysis through the Rayleigh scattering method (RSM)

Radar traces from the pulseEKKO pulsed radar system were processed for each test. A denoising step was applied by means of low-pass (i.e., 1000 MHz) and high-pass (i.e., 150 MHz) filters. Subsequently, a fast Fourier transform (FFT) was used for retrieving the frequency spectrum of the radar signal, and the frequency peak f_P of each spectrum, namely, the frequency of the maximum amplitude, was then extracted. To enhance the accuracy of the processing, a number of 20 traces per sample was collected, so that a more stable value of f_P could be achieved for each soil sample by averaging as follows:

$$\overline{f_p} = \frac{1}{n}\sum_{i=1}^{n} f_{P,i} \tag{20}$$

with n being the total amount of i replicas, and $f_{P,i}$ being the frequency of the i^{th} spectrum. Such operation is useful in case of instability in the values of f_P extracted by FFT within the same soil sample, i.e., when the shift of the spectrum peak approaches to be sensitive to an increase of water content. Further insights on the application of super-resolution techniques in the spectral domain are discussed in Benedetto and Tosti (2013b).

An overview on the behavior describing the frequency modulations of signal spectra can be seen in Figure 6a-f. Theoretical motivations and empirical observations on this phenomenon can be found in literature for natural soils and compacted loose materials (e.g., Benedetto 2010), as well as for concrete materials (e.g., Laurens 2005).

It is evident how the frequency peak moves systematically to lower values of frequency, regardless of the grain size and the presence of clay, which however are fundamental to provide a more comprehensive interpretation of such occurrence. Table 4 lists the measured values of frequency peaks, case by case.

FIGURE 6. 3D representation of the frequency spectra modulation for the soil types investigated from dry to saturated conditions. Clay-free conditions – A1 (a), A2 (b), A3 (c) – and 15% of clay conditions – A1 (d), A2 (e), A3(f) –.

TABLE 4. Measured values of frequency spectra peaks f_P [Hz × 10^8] for 0% and 15% clay samples from dry to saturated conditions.

The overall behavior in both clay-free and clay-rich conditions in terms of peaks shifting is represented, respectively, in Figure 7a and 7b. In addition and according to Equation (18), the calibrated A and B parameters along with the relevant regression coefficients for volumetric water content prediction are listed in Table 5. As it can be seen, the mean squares fitting linear curves are characterized by relatively high correlation coefficients R^2, especially for the finer-grained soil types A2 and A3 with 15% of clay content.

FIGURE 7. Trend of values of frequency spectra peak (f_P) across the range of moisture contents investigated for clay-free (a), and clay-rich soil samples (b).

TABLE 5. Values of regression coefficients in Equation (18).

Numerical data show how the frequency shift occurs, across the range of moisture investigated, with two main rates of displacement, whose dimensions vary according to the grain size and clay content of the samples. Basically, a lower shift of frequency peaks is firstly observed (i.e., low amounts of water content). Secondly (i.e., increasing amounts of water content), more remarkable displacements are noticed.

In both clay-free and clay-rich conditions, it can be noticed how the coarser is the grain size of the soil the lower is the amount of moisture by which the aforementioned two steps of displacement occur. Considering clay-free conditions (Figure 6a-c), the range of frequency peaks variation $\Delta f_{P\ \text{A1-0\% clay}}$ for the A1 soil type reaches a water content of θ = 6.71% (Sample 7)

at the beginning of the second main step of displacement (relevant $\Delta f_{P\ \text{A1-0\% clay}} = 4.11\times10^8$ Hz). The same step begins at θ = 21.43% (Sample 16) for the A2 soil type (relevant $\Delta f_{P\ \text{A2-0\% clay}} = 3.92\times10^8$ Hz), while lower displacements are reached for the A3 soil type, being the last moisture value θ equals to 26.63% (Sample 27) with a significantly lower range of variation of frequency peaks (relevant $\Delta f_{P\ \text{A3-0\% clay}} = 2.15\times10^8$ Hz).

In clay-rich conditions (Figure 6d-f), numerical results demonstrate how this occurrence is broadly more attenuated, although its strong dependence on the grain size of the soil samples is yet confirmed. Indeed, despite the lower Δf_P intervals, much higher volumetric water contents than in clay-free conditions are observed within this range, and the finer is the grain size the higher is the amount of moisture. In more details, such range of variation $\Delta f_{P\ \text{A1-15\% clay}}$ measures 3.14×10^8 Hz for the A1 clay-rich soil type, and it is reached in a wide field of moisture (θ = 23.95% - Sample 32). Within the A2 clay-rich soil samples, the highest $\Delta f_{P\ \text{A2-15\% clay}}$ measures 0.59×10^8 Hz with a relevant water content θ = 27.13% (Sample 41), while $\Delta f_{P\ \text{A3-15\% clay}} = 1.57\times10^8$ Hz and θ = 29.40% (Sample 51) are noticed for the A3 clay-rich finer soil type.

Such overall behavior can find reasonable explanations by relating the contribution of water, clay and grain size of the undisturbed material. Several transition water states occur when starting to add water in a system of dry soil particles, namely, tightly bound and loosely bound adsorption water, capillary water, and free water (Mitchell 1992). According to this, different rates of polarization of the water dipoles occur, with the grain size and mineralogy of soils playing an important role in the modes of such occurrence (Saarenketo 1998). In case of A1 clay-rich soil samples (Figure 6d), it is found the widest experimental heterogeneity between particles, i.e., among the undisturbed material (i.e., grain size 4-8 mm) and the bentonite clay. When adding low amounts of water into a dry system composed by many particles from these two types of population, both the gravel and the clay particles retain water by molecular forces, therefore it is expected that the water dipoles are not fully-polarized by the EM field. In these cases, lower variations of the frequency peaks of the spectra can be noticed. When increasing the water content, clay particles continue to retain moisture, due to their swelling properties,

without undergoing any polarization, while gravel grains begin to loose water molecules, which in contrast start to polarize. In such conditions, slightly higher variation of the frequency peaks of the spectra can be observed. On the other hand, if the water amount added is considerable, both the two types of population take part in the polarization of water dipoles, since a large amount of clay particles begin to polarize all together. Such condition reflects in the highest rate of variation of the frequency spectra peaks, as a result of a sudden amount of polarized water dipoles. In case of finer-grained particles with 15% of clay content, such as the A3 clay-rich soil samples (Figure 6f), the above two populations are instead characterized by particle sizes very close each other, thereby the A3 fine sand is capable to retain higher amounts of water, as well as losing more gradually water molecules. In line with this, such "shifting" behavior involving the peaks of frequency spectra is much more attenuated.

When considering clay-free conditions (Figure 6a-c) with a unique population of soil particles and a relatively homogeneous grain size, the shift of the frequency peaks of spectra occurs more rapidly and linearly, although a higher disorder of the several frequency components of the spectra can be broadly observed.

SUMMARY OF THE MAIN RESULTS

Permittivity-based methods

General considerations

- Higher water contents reflect into increasing values of relative dielectric permittivity.
- Considerable lower permittivity values in clayey soil samples are observed with respect to clay-free samples.
- Similar permittivity values are returned with the four processing methods used in this study in case of clayey samples. Slighter variations of permittivity between dry-member and end-member cases are also encountered.

Clay-free samples

- The agreement of the processing techniques used in this study in θ estimate is highly dependent on the soil texture: the lower is the grain size, the closer are the relative dielectric permittivity values.
- The FWI technique has a higher sensitivity than the other permittivity-based processing methods to single out the low threshold between loosely bound molecular and capillary water in coarser-grained materials (i.e., A1 and A2 soil types) and determining reliable values of moisture within the whole depth domain investigated.
- The SRM seems to be more suited for characterising the loosely bound water content of the upper (surface) part of the samples in coarser-grained materials (i.e., A1 and A2 soil types) when moisture conditions are not saturated.
- The VMF approach used herein does not provide worthwhile information for distinguishing any transition water states due to the theoretical assumptions of the model itself, which diverts from the real grain size structure of the soils investigated.

Clay-rich samples

- The Topp's general relationship returns higher values of relative dielectric permittivity than the processing techniques employed here for all the three types of soil.
- Good results consistency is observed between the FWI and the SRM methods within all the three types of soil investigated due to the clay ability of retaining water and fairly homogenising its content within the soil volume.
- In most cases, the VMF approach overestimates the permittivity values with respect to FWI and SRM, since the rates of tightly bound water to clay content are not taken into account by its theoretical model.

Rayleigh scattering method

- When increasing the water content, the peak of the frequency spectra of the signals moves systematically to lower values of frequency, regardless of the grain size and the clay content.
- In both clay-free and clay-rich samples, the highest linear correlation coefficients in frequency peaks shifting vs VWC relationships are found for finer-grained clayey soil types (i.e., A2 and A3)
- Two main rates of displacement for the shifting of the frequency spectra peaks are observed. The occurrence and dimension of such behaviour vary according to the grain size and the clay content of the soil samples.
- In both clay-free and clay-rich samples, the coarser is the grain size of the soil, the lower is the amount of water whereby the frequency peaks displacement takes place.
- The frequency spectra peaks displacement is more attenuated in clay-rich than in clay-free conditions. Anyhow, in clayey conditions, the wider is the grain size heterogeneity between the undisturbed soil and the clay particles (i.e., A1 soil type), the higher is the rate of frequency displacement.

CONCLUSIONS

This study is motivated by the need to understand the dielectric behavior of clayey subgrade soils and unbound load-bearing layers using ground-penetrating radar. Data from two different radar systems are analyzed at the laboratory scale of investigation for three types of soil classified by AASHTO as A1, A2, and A3 in both clay-free and clay-rich conditions (15% by weight of clay) under different water contents.

Several permittivity-based methods were used for data processing, namely, the time-domain signal picking technique, the full-wave inversion method, the surface reflection method, and the volumetric mixing formulae. An implementation of the time domain signal picking technique within the full-wave inversion method has been also presented. Considerably lower values of

dielectric permittivity are observed in clayey samples with respect to clay-free conditions. Permittivity estimates very close to each other are also detected between dry-member and end-member (i.e., saturated) cases by the four approaches. On the contrary, considerable differences of dielectrics are detected in clay-free cases. Comparisons between the above dielectrics and the volumetric water contents of samples, gravimetrically determined, highlight considerable differences among the full-wave technique and the other approaches. A very good capability of this method in evaluating permittivity values of unsaturated coarse-grained materials in clay-free conditions is shown. Overall, differences in permittivity estimates decrease for finer grain sizes, such that the full-wave inversion traces relatively well the trend of the Topp's general relationship for the A3 soil type. The surface reflection method and the volumetric mixing approach do not perform well in characterizing the overall volumetric water contents in 10.5 cm thick formworks.

Concerning clay-rich soil samples, a very good agreement in the trend of the full-wave inversion approach and the surface reflection method is noticed, due to the swelling properties of clay, which creates a relatively homogeneous mixtures of the multi-phase components of the soil samples, such that low changes of permittivity throughout the thickness of the formwork are encountered. In such clayey conditions, the Topp's general expression broadly overestimates the values of soil permittivity. By a lower entity, considerable overestimates are also encountered using the volumetric mixing approach.

The ability to detect clay in soils was also investigated using a Rayleigh-based scattering technique, which relies on analyses carried out in the spectral domain of the GPR signal. The results demonstrate a strong contribution of water, clay and grain size of the undisturbed material on the occurrence of scattering phenomena. Higher variations in the range of frequency spectra peaks are noticed in clay-free soil samples with respect to clay-rich conditions, being this frequency-dependent behavior more rapid and linear, despite the overall higher disorder of the several frequency components of the spectra. On the contrary, clay-rich soils exhibit simpler spectral behaviors, and frequency shifts develop across higher amounts of water content, due the

swelling properties of clay. Soil-specific regression functions are proposed for estimating water content as a function of the peaks of frequency spectra.

ACKNOWLEDGEMENTS

The research was supported by the ASTRI project, financed by Roma Tre University under the Framework Program for "Progetto di internazionalizzazione della ricerca e della formazione della ricerca". A strong support was also provided by the Delft University of Technology, for enabling the use of facilities, materials, and laboratory sites. The authors are thankful to Dr. Karl-Heinz Wolf for permission to use the laboratory sites, as well as to Ing. Karel Heller and Ing. Wim Verwaal, for their invaluable help and support.

This work also benefited from the network activities carried out within the EU funded COST Action TU1208 "Civil Engineering Applications of Ground Penetrating Radar".

References

Abdi, M.R., Sadrnejad, A.,. Arjomand, M.A., 2009. Strength enhancement of clay by encapsulating geogrids in thin layers of sand. Geotext. Geomembranes. 27, 447-455.

Abusharar, S.W., Han, J., 2011. Two-dimensional deep-seated slope stability analysis of embankments over stone column-improved soft clay. Eng. Geol. 120, 103-110.

Al-Qadi I.L. and Lahouar S. 2004. Use of GPR for thickness measurement and quality control of flexible pavements. Journal of the Association of Asphalt Paving Technologists 73, 501–528.

American Association of State Highway and Transportation Officials (AASHTO), 2011. Roadside Design Guide, 4th edition. AASHTO, Washington, DC.

Benedetto A. 2010. Water content evaluation in unsaturated soil using GPR signal analysis in the frequency domain. Journal of Applied Geophysics 71, 26–35. doi: 10.1016/j.jappgeo.2010.03.001.

Benedetto A., Benedetto F. and Tosti F. 2012a. GPR applications for geotechnical stability of transportation infrastructures. Nondestructive Testing And Evaluation 27(3), 253–262. doi: 10589759.2012.694884.

Benedetto A., Manacorda G., Simi A. and Tosti F. 2012b. Novel perspectives in bridges inspection using GPR. Nondestructive Testing And Evaluation 27(3), 239–251.

Benedetto A. and Tosti F. 2013a. Inferring bearing ratio of un-bound materials from dielectric properties using GPR: the case of Runaway Safety Areas. In: *Proceedings of the Airfield and Highway Pavement 2013 Conference*, Los Angeles, California, USA, pp. 1336-1347. doi: 10.1061/9780784413005.113.

Benedetto A., D'Amico F. and Tosti F. 2014a. Improving safety of runway overrun through the correct numerical evaluation of rutting in Cleared and Graded Areas. Safety Science 62, 326–338. doi: 10.1016/j.ssci.2013.09.008.

Benedetto, A, Tosti, F., Pajewski, L., D'Amico, F., and Kusayanagi, W. 2014b. FDTD Simulation of the GPR Signal for Effective Inspection of Pavement Damages. In: *Proceedings*

of the Fifteenth International Conference on Ground Penetrating Radar, Bruxelles, Belgium, pp. 513-518.

Benedetto, A., Tosti, F., Ortuani, B., Giudici, M., and Mele, M. 2015. Mapping the spatial variation of soil moisture at the large scale using GPR for pavement applications. Near Surface Geophysics. 13 (3), 269–278. Doi: 10.3997/1873-0604.2015006.

Benedetto F. and Tosti F. 2013b. GPR spectral analysis for clay content evaluation by the frequency shift method. Journal of Applied Geophysics 97, 89–96. doi: 10.1016/j.jappgeo.2013.03.012.

Beroya, M.A.A., Aydin, A., Katzenbach, R., 2009. Insight into the effects of clay mineralogy on the cyclic behavior of silt–clay mixtures. Eng. Geol. 106, 154-162.

Birchack J.R., Gardner C. G., Hipp J.E. and Victor M. 1974. High dielectric constant microwave probes for sensing soil moisture. Proceedings of the IEEE. Vol 62. No. 1.

Bohren CF, Huffman D. Absorption and scattering of light by small particles. New York: John Wiley; 1983.

Daniels D.J. 2004. Ground Penetrating Radar. The Institution of Electrical Engineers, London.

Davis, J.L., Annan, A.P., 2002. Ground penetrating radar to measure soil water content, in Dane, J.H. and Topp, G.C. (eds), Methods of Soil Analysis, Part 4, Soil Science Society of America (SSSA), pp. 446-463.

De Benedetto, D., Castrignano, A., Sollitto, D., Modugno, F., Buttafuoco, G., Papa, G.L., 2012. Integrating geophysical and geostatistical techniques to map the spatial variation of clay. Geoderma, 171-172, 53-63.

Dobson, M.C., Ulaby, F.T., Hallikainen, M.T., El-Rayes, M.A., 1985. Microwave dielectric behavior of wet soil. Part II. Dielectric mixing models. IEEE Transactions on Geoscience and Remote Sensing 23, 35–46.

Drude, P., 1902. The theory of Optics. Longmans, Green, and Co, New York, 268–396.

Dudoignon, P., Causseque, S., Bernard, M., Hallaire, V., Pons, Y., 2007. Vertical porosity profile of a clay-rich marsh soil. Catena 70, 480-492.

Fellner-Feldegg, H., 1969. Measurement of dielectrics in time domain. The Journal of Physical Chemistry 73, 616–623.

Gómez-Ortiz, D., Martín-Crespo, T., Martín-Velázquez, S., Martínez-Pagán, P., Higueras, H., Manzano, M., 2010. Application of ground penetrating radar (GPR) to delineate clay layers in wetlands. A case study in the Soto Grande and Soto Chico watercourses, Doñana (SW Spain). Journal of Applied Geophysics, 72 (2), 107-113.

Gorriti A.G. and Slob E.C. 2005. Synthesis of all known analytical permittivity reconstruction techniques of nonmagnetic materials from reflection and transmission measurements. IEEE Geoscience and Remote Sensing Letters, Vol. 2, No. 4, doi: 10.1109/LGRS.2005.853199

Ho, K.C., Gader, P.D., Wilson, J.N., 2004. Improving landmine detection using frequency domain features from ground penetrating radar. Proceedings. 2004 IEEE International Geoscience and Remote Sensing Symposium, IGARSS '04, Vol. 3, pp. 1617–1620.

Huisman J.A., Hubbard S.S., Redman J.D. and Annan A.P. 2003. Measuring soil water content with ground penetrating radar: a review. Vadose Zone Journal 2, 476–491. doi: 10.2113/2.4.476.

Huston D.R., Hu J., Maser K., Weedon W. and Adam C. 1999. Ground penetrating radar for concrete bridge health monitoring applications. In: *Proceedings of SPIE* 3587, pp. 170-179. doi:10.1117/12.339922.

Lambot S., Slob E.C., van den Bosch I., Stockbroeckx B. and Vanclooster M. 2004a. Modeling of ground-penetrating radar for accurate characterization of subsurface electric properties. IEEE Transactions on Geoscience and Remote Sensing 42, 2555–2568. doi: 10.1109/TGRS.2004.834800.

Lambot, S. , Rhebergen, J., van den Bosch, I., Slob, E.C., and Vanclooster, M. 2004b. Measuring the soil water content profile of a sandy soil with an off-ground monostatic ground penetrating radar, Vadose Zone Journal 3, 1063–1071. doi: 10.2113/3.4.1063.

Lambot S., Weihermüller L., Huisman J.A., Vereecken H., Vanclooster M. and Slob E.C. 2006. Analysis of air-launched ground-penetrating radar techniques to measure the soil surface water content. Water Resources Research 42(11), W11403. doi: 10.1029/2006WR005097.

Laurens, S., Balayssac, J-P., Rhazi, J., Klysz, G., Arliguie, G. 2005. Non-destructive evaluation of concrete moisture by GPR: Experimental study and direct modeling. Materials and Structures. 38(283), 827–832.

Lichtenecker, K., Rother, K., 1931. Die herleitung des logarithmischen mischungsgesetzes aus allgemeinen prinzipien der stätionaren strömung. Physik Z. 32, 255–260.

Lyon, T.L., Buckman, H.O., 1937. The Nature and Properties of Soils. Macmillan, New York. p. 391.

Mahmoudzadeh, M.R., André, F., van Wesemael, B., Lambot, S., 2011. Clay content and soil moisture mapping using on-ground time-domain GPR. In Proceedings of the 2nd Workshop on Proximal Soil Sensing, Montreal, Canada, May 15-18. p. 44-47.

Mie, G., 1908. Beiträge zur Optik trüber Medien, speziell kolloidaler Metallösungen. Annalen der Physik 330, 377.

Minet J, Wahyudi A., Bogaert P., Vanclooster M. and Lambot S. 2011. Mapping shallow soil moisture profiles at the field scale using full-wave inversion of ground penetrating radar data. Geoderma 161, 225–237. doi: 10.1016/j.geoderma.2010.12.023.

Miqueleiz, L., Ramirez, F., Seco, A., Nidzam, R.M., Kinuthia, J.M., Abu Tair, A., Garcia, R., 2012. The use of stabilised Spanish clay soil for sustainable construction materials. Eng. Geol. 133-134, 9-15.

Mitchell, J.K., 1992. Fundamentals of Soil Behavior, 2nd edn. Wiley, New York. p. 437.

Narayana, P.A., Ophir, J., 1983. On the frequency dependence of attenuation in normal and fatty liver. IEEE Transactions on sonics and ultrasonics SU30 6, 379–383.

Odeh, I.O.A., McBratney, A.B., 2000. Using AVHRR images for spatial prediction of clay content in the lower Namoi Valley of eastern Australia. Geoderma 97, 237-254.

Pakbaz, M.S., Alipour, R., 2012. Influence of cement addition on the geotechnical properties of an Iranian clay. Appl. Clay Sci. 67-68, 1-4.

Patriarca, C., Lambot, S., Mahmoudzadeh, M.R., Minet, J., Slob, E.C., 2011. Reconstruction of sub-wavelength fractures and physical properties of masonry media using full-waveform inversion of proximal penetrating radar. Journal of Applied Geophysics 74, 26–37. doi:10.1016/j.jappgeo.2011.03.001

Patriarca C., Tosti F., Velds C., Benedetto A., Lambot S. and Slob E.C. 2013. Frequency dependent electric properties of homogeneous multi-phase lossy media in the ground-penetrating radar frequency range. Journal of Applied Geophysics 97, 81–88. doi: 10.1016/j.jappgeo.2013.05.003.

Redman J., Davis J., Galagedara L. and Parkin G. 2002. Field studies of GPR air launched surface reflectivity measurements of soil water content. In: *Proceedings of the Ninth International Conference on Ground Penetrating Radar*, Santa Barbara, California, USA. S. Koppenjan and K. Lee, Eds. 4758, pp. 156-161.

Richard, G., Cousin, I., Sillon, J.F., Bruand, A., Guérif, J., 2001. Effect of compaction on the porosity of a silty soil: influence on unsaturated hydraulic properties. Eur. J. Soil Sci. 52, 49-58.

Robinson, D.A., Phillips, C.P., 2001. Crust development in relation to vegetation and agricultural practice on erosion susceptible, dispersive clay soils from central and southern Italy. Soil Till. Res. 60, 1-9.

Robinson, D.A., Campbell, C.S., Hopmans, J.W., Hornbuckle, B.K., Jones, S.B., Knight, R., Ogden, F., Selker, J. Wendroth, O., 2008. Soil moisture measurement for ecological and hydrological watershed-scale observatories: a review. Vadose Zone Journal 7 (1), 58–389.

Roth, K., Schulin, R., Fluhler, H., Attinger, W., 1990. Calibration of time domain reflectometry for water content measurement using composite dielectric approach. Water Resources Research 26, 2267–2273.

Saarenketo, T., 1998. Electrical Properties of Water in Clay and Silty Soils. Journal of Applied Geophysics 40(1–3), 73–88.

Saarenketo, T., Scullion, T., 2000. Road evaluation with ground penetrating radar. J. Appl. Geophys., 43 (2), 119-138.

Scullion T., Lau C.L. and Chen Y. 1994. Pavement evaluations using ground penetrating radar. International Conference on Ground Penetrating Radar. In: *Proceedings of the Fifth International Conference on Ground Penetrating Radar*, Kitchener, Ontario, Canada, pp. 449-463.

Scullion, T., Saarenketo, T., 1997. Using suction and dielectric measurements as performance indicators for aggregate base materials. Transportation Research Record 1577, TRB, national Research Council, Washington, D.C., pp. 37-44.

Serbin G. and Or D. 2004. Ground-penetrating radar measurement of soil water content dynamics using a suspended horn antenna. IEEE Transactions on Geoscience and Remote Sensing, Vol. 42, No. 8. doi: 10.1109/TGRS.2004.831693.

Slob, E.C., Fokkema, J.T., 2002. Interfacial dipoles and radiated energy, Subsurface Sens. Technol. Appl., 3(4), 399 – 419.

Slob E.C., Sato M. and Olhoeft G., 2010. Surface and borehole ground-penetrating-radar developments. Geophysics 75(5), A103-A120. doi: 10.1190/1.3480619.

Srasra, E., Bergaya, F., Fripiat, J.J., 1994. Infrared spectroscopy study of tetrahedral and octahedral substitutions in an interstratified illite-smectite clay. Clays and Clay Minerals, 42 (3), pp. 237-241.

Topp G.C., Davis J.L. and Annan A.P. 1980. Electromagnetic determination of soil water content: measurements in coaxial transmission lines. Water Resources Research 16, 574–582. doi: 10.1029/WR016i003p00574.

Tosti, F., Benedetto, A., Calvi, A. 2014a. Efficient air-launched ground-penetrating radar inspections in a large-scale road network. In Proc. of the 3rd International Conference on Transportation Infrastructure, Pisa, Italy, Apr. 2014, pp. 703–709.

Tosti, F., Adabi, S., Pajewski, L., Schettini, G., and Benedetto, A. 2014b. Large-scale analysis of dielectric and mechanical properties of pavement using GPR and LFWD. In: *Proceedings of*

the Fifteenth International Conference on Ground Penetrating Radar, Bruxelles, Belgium, pp. 268-273.

Tosti F., Patriarca C., Slob E.C., Benedetto A. and Lambot S. 2013. Clay content evaluation in soils through GPR signal processing. Journal of Applied Geophysics 97, 69–80. doi: 10.1016/j.jappgeo.2013.04.006.

Triantafilis, J., Lesch, S.M., 2005. Mapping clay content variation using electromagnetic induction techniques. Comput. Electron. Agr. 46, 203-237.

Uzan, J., 1998. Characterization of clayey subgrade materials for mechanistic design of flexible pavements. Transportation Research Record, (1629), pp. 189-196.

van der Kruk J. and Slob E.C. 2004. Reduction of reflections from above surface objects in GPR data. Journal of Applied Geophysics 55, 271–278. doi: 10.1016/j.jappgeo.2004.02.002.

Viscarra Rossel, R.A., Cattle, S.R., Ortega, A., Fouad, Y., 2009. In situ measurements of soil colour, mineral composition and clay content by vis–NIR spectroscopy. Geoderma 150, 253-266.

Wagner, W., Blöschl, G., Pampaloni, P., Calvet, J.C., Bizzarri, B., Wigneron, J.P., Kerr, Y., 2007. Operational readiness of microwave remote sensing of soil moisture for hydrologic applications. Nordic Hydrology 38 (1), 1–20.

Wobshall, D. 1978. A frequency shift dielectric soil moisture sensor. IEEE Geosci. Electronics, Vol. GE16, 112-118.

Wuddivira, M.N., Robinson, D.A., Lebron, I., Bréchet, L., Atwell, M., De Caires, S., Oatham, M., Jones, S.B., Abdu, H., Verma, A.K., Tuller, M., 2012. Estimation of soil clay content from hygroscopic water content measurements. Soil Science Society of America Journal, 76 (5), pp. 1529-1535.

List of captions

FIGURE 1 Measured Green's function in the time domain $g^{\uparrow}_{xx,mea}(t)$ and time delay Δt_1 between air-medium and medium-PEC interfaces.

FIGURE 2. Flowchart representing the implementation of the TDSP technique within the FWI approach.

FIGURE 3. Test devices and equipment a) SFCW radar set-up using a vector network analyzer HP 8573C (Hewlett Packard Company, USA) and a linear polarized double-ridged broadband TEM horn BBHA 9120 A (Schwarzbeck Mess-Elektronik, Germany), in a mono-static configuration. b) PulseEKKO PRO 500 pulsed radar system, manufactured by Sensors & Software Inc., Canada.

TABLE 1. Relative dielectric permittivity values retrieved using different processing methods for 0% and 15% clay samples.

FIGURE 4. Measured and modeled Green's functions in the frequency (amplitude $|G^{\uparrow}_{xx}|$ and phase $\angle G^{\uparrow}_{xx}$) and time ($g^{\uparrow}_{xx}$) domain. (a) soil sample 23 (A3, clay = 0%, θ = 10.9%); (b) soil sample 45 (A3, clay = 15%, θ = 9.7%).

TABLE 2. Normalized Root Mean Square Deviation (NRMSD) values in clay-free soil samples by comparing the different permittivity-based methods.

FIGURE 5. Plots of volumetric water contents θ vs dielectric permittivity values ε_r by different permittivity-based methods in clay-free – A1 (a), A2 (b), A3 (c) – and 15% of clay conditions – A1 (d), A2 (e), A3(f) –.

TABLE 3. Normalized Root Mean Square Deviation (NRMSD) values in clay-rich soil samples (15% of clay) by comparing the different permittivity-based methods.

FIGURE 6. 3D representation of the frequency spectra modulation for the soil types investigated from dry to saturated conditions. Clay-free conditions – A1 (a), A2 (b), A3 (c) – and 15% of clay conditions – A1 (d), A2 (e), A3(f) –.

TABLE 4. Measured values of frequency spectra peaks f_P [Hz × 10^8] for 0% and 15% clay samples from dry to saturated conditions.

FIGURE 7. Trend of values of frequency spectra peak (f_P) across the range of moisture contents investigated for clay-free (a), and clay-rich soil samples (b).

TABLE 5. Values of regression coefficients in Equation (18).

Figures

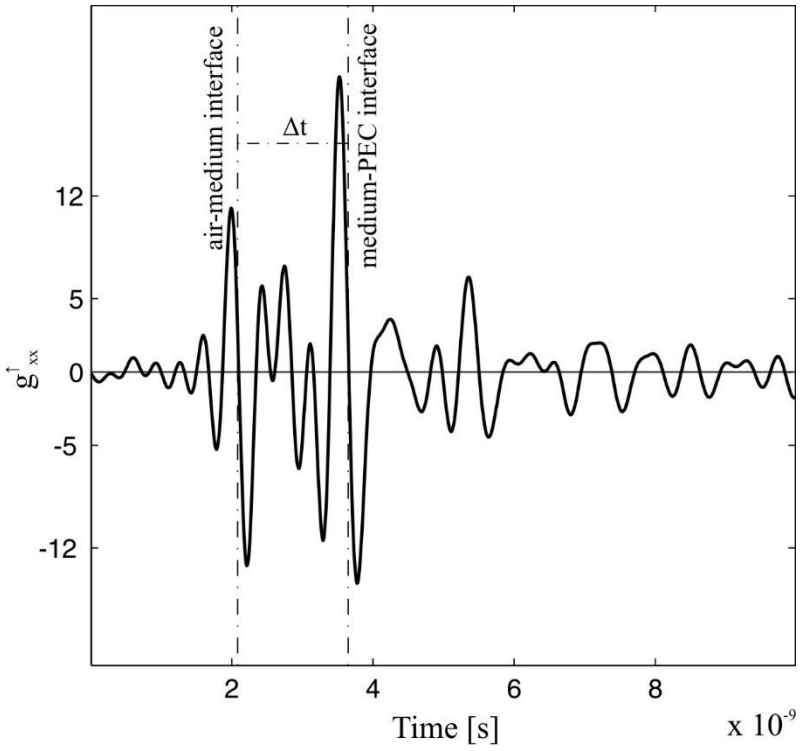

FIGURE 1 Measured Green's function in the time domain $g^{\uparrow}_{xx,meas}(t)$ and time delay Δt_1 between air-medium and medium-PEC interfaces.

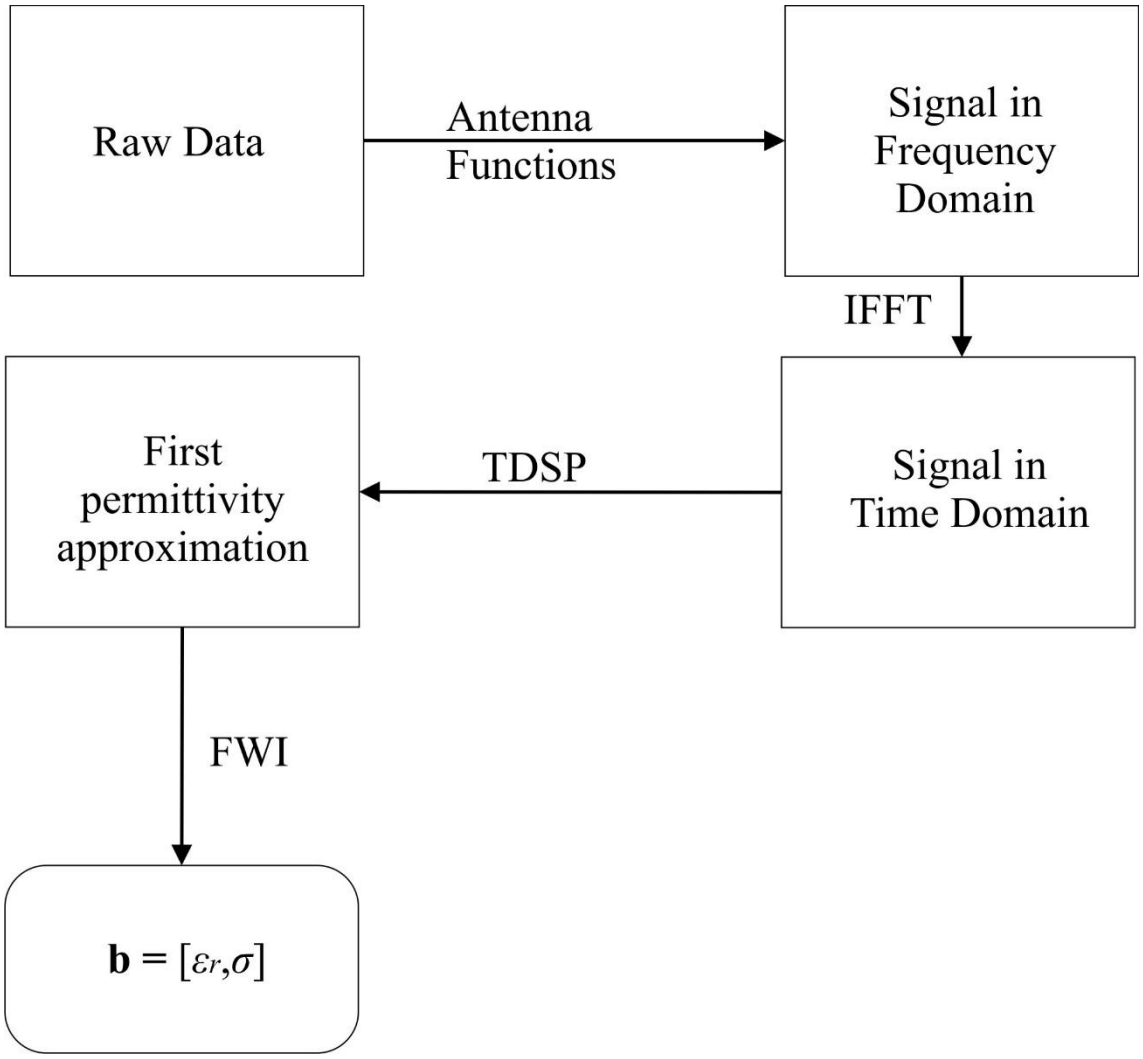

FIGURE 2. Flowchart representing the implementation of the TDSP technique within the FWI approach.

FIGURE 3. Test devices and equipment a) SFCW radar set-up using a vector network analyzer HP 8573C (Hewlett Packard Company, USA) and a linear polarized double-ridged broadband TEM horn BBHA 9120 A (Schwarzbeck Mess-Elektronik, Germany), in a mono-static configuration.

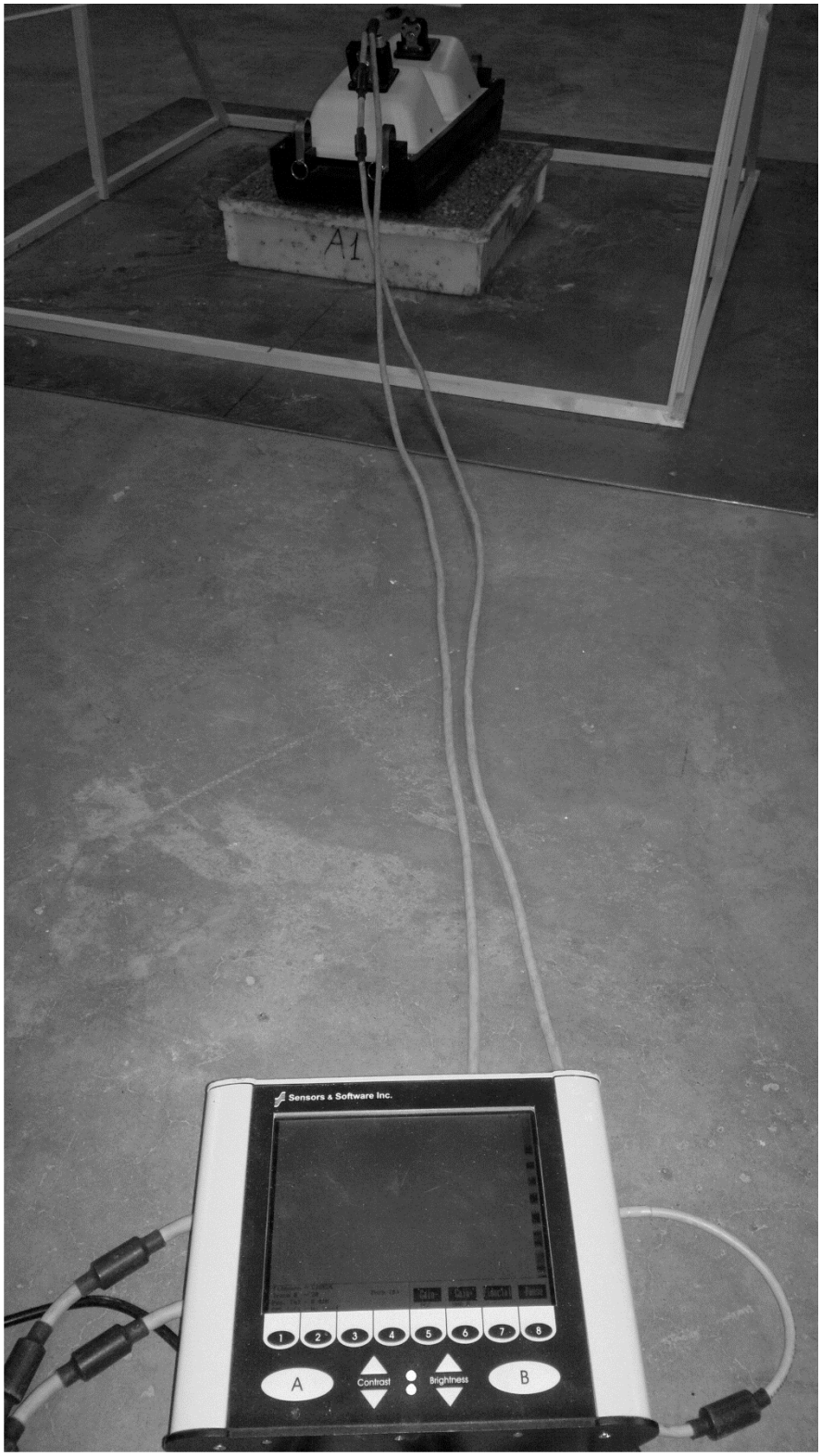

FIGURE 3. Test devices and equipment b) PulseEKKO PRO 500 pulsed radar system, manufactured by Sensors & Software Inc., Canada.

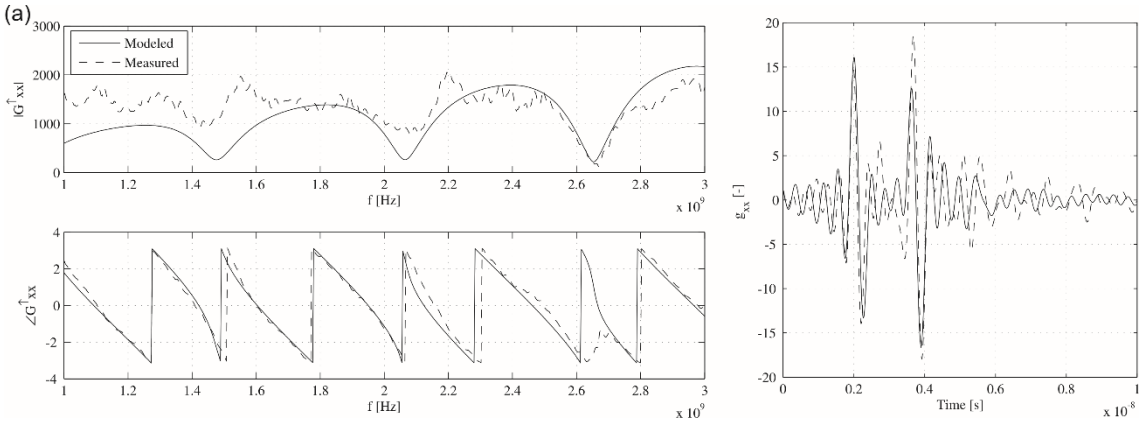

FIGURE 4. Measured and modeled Green's functions in the frequency (amplitude $|G_{xx}^{\uparrow}|$ and phase $\angle G_{xx}^{\uparrow}$) and time ($g_{xx}^{\uparrow}$) domain. (a) soil sample 23 (A3, clay = 0%, θ = 10.9%)

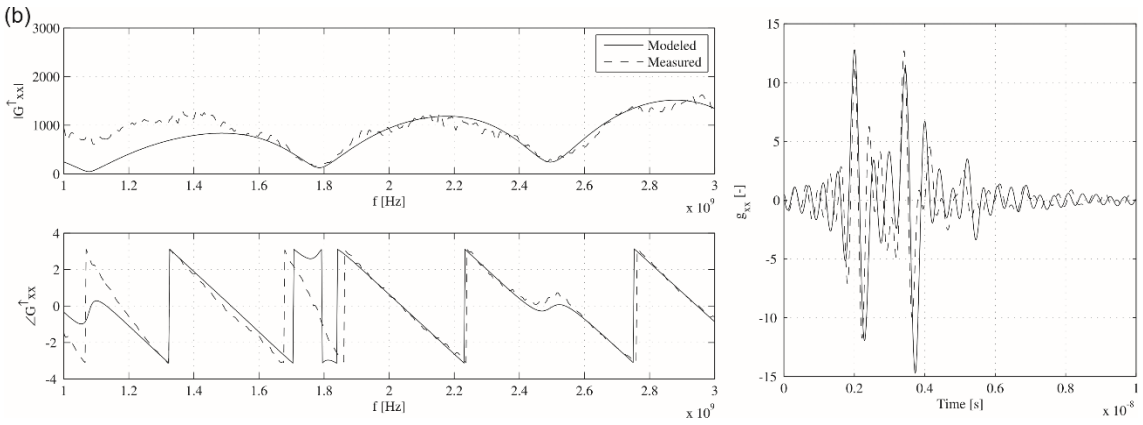

FIGURE 4. Measured and modeled Green's functions in the frequency (amplitude $|G_{xx}^{\uparrow}|$ and phase $\angle G_{xx}^{\uparrow}$) and time ($g_{xx}^{\uparrow}$) domain. (b) soil sample 45 (A3, clay = 15%, θ = 9.7%).

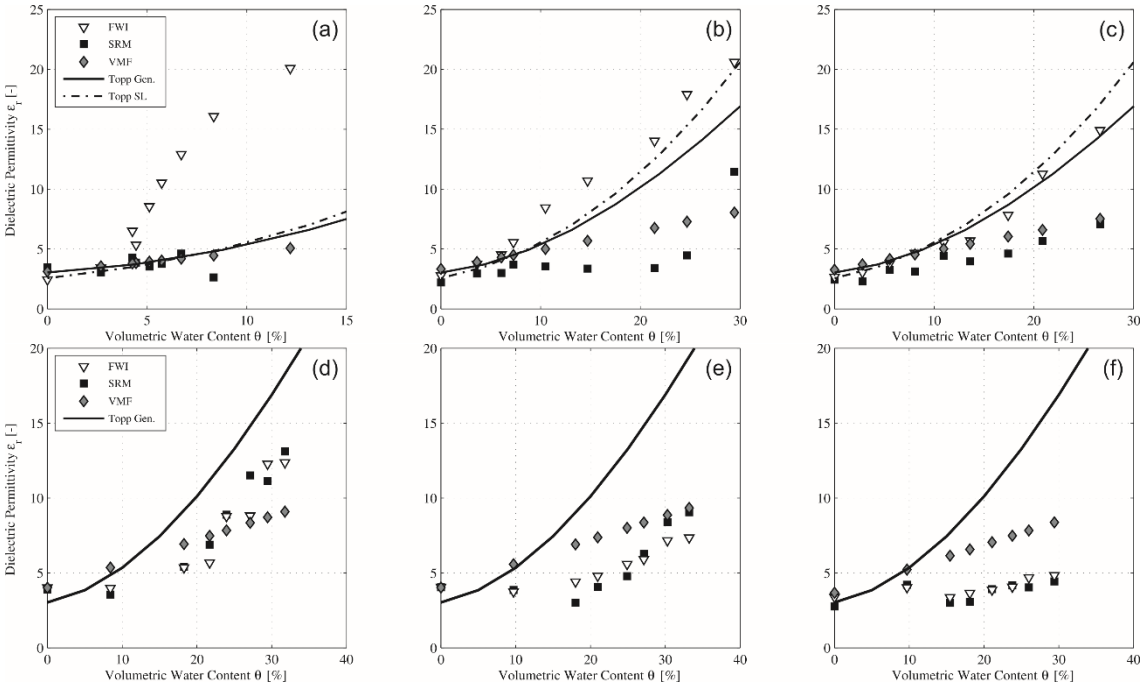

FIGURE 5. Plots of volumetric water contents θ vs dielectric permittivity values ε_r by different permittivity-based methods in clay-free – A1 (a), A2 (b), A3 (c) – and 15% of clay conditions – A1 (d), A2 (e), A3(f) –.

(a)

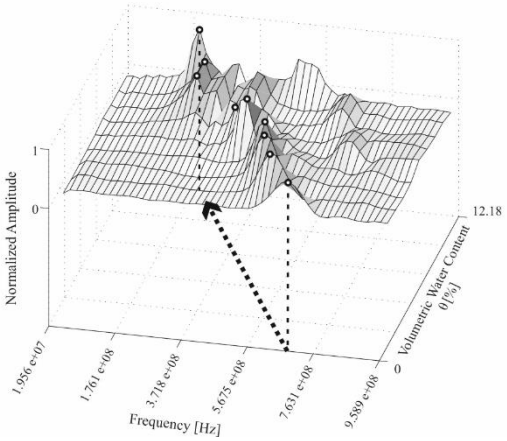
Normalized Amplitude
1
0
1.956 e+07
1.761 e+08
3.718 e+08
5.675 e+08
7.631 e+08
9.589 e+08
Frequency [Hz]
0
12.18
Volumetric Water Content θ [%]

(b)

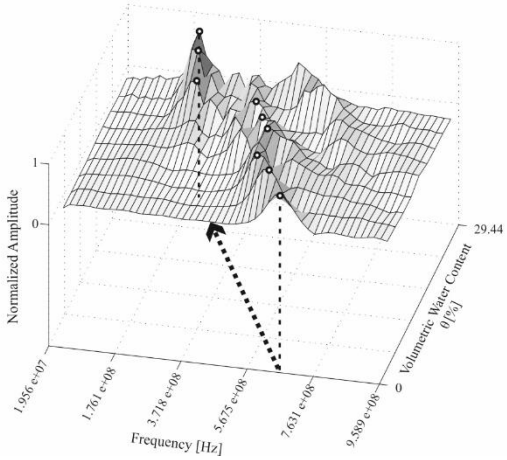
Normalized Amplitude
1
0
1.956 e+07
1.761 e+08
3.718 e+08
5.675 e+08
7.631 e+08
9.589 e+08
Frequency [Hz]
0
29.44
Volumetric Water Content θ [%]

(c)

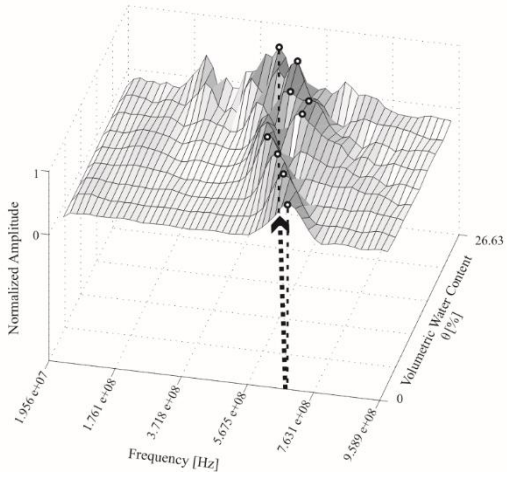
Normalized Amplitude
1
0
1.956 e+07
1.761 e+08
3.718 e+08
5.675 e+08
7.631 e+08
9.589 e+08
Frequency [Hz]
0
26.63
Volumetric Water Content θ [%]

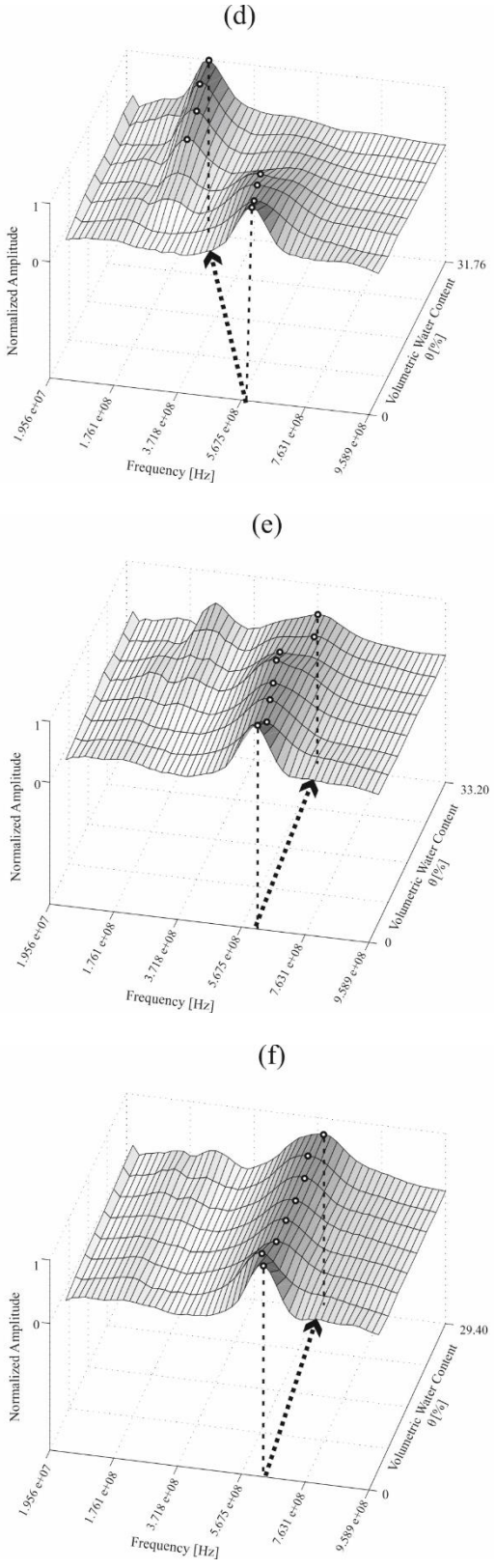

FIGURE 6. 3D representation of the frequency spectra modulation for the soil types investigated from dry to saturated conditions. Clay-free conditions – A1 (a), A2 (b), A3 (c) – and 15% of clay conditions – A1 (d), A2 (e), A3(f) –.

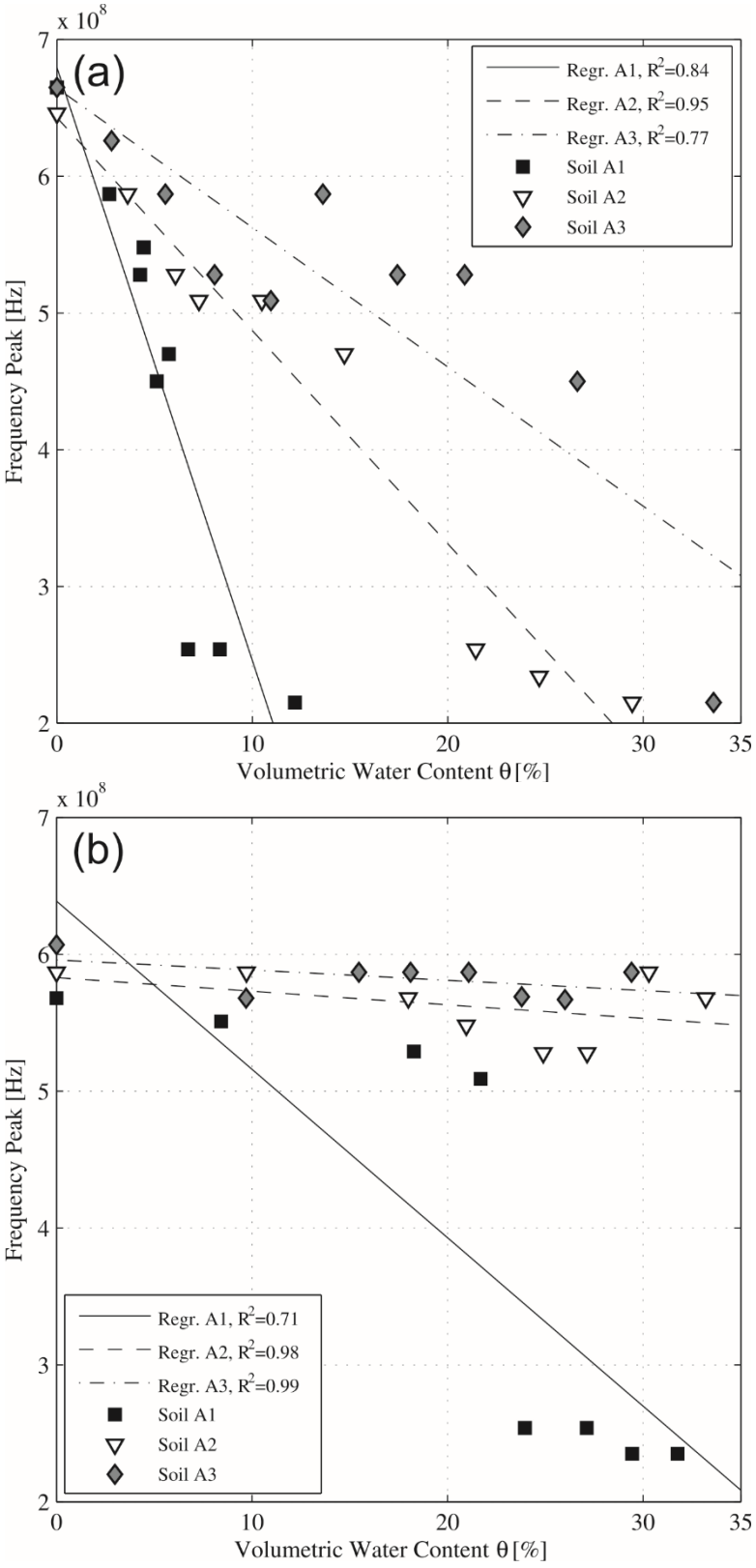

FIGURE 7. Trend of values of frequency spectra peak (f_P) across the range of moisture contents investigated for clay-free (a), and clay-rich soil samples (b).

Tables

TABLE 1. Relative dielectric permittivity values retrieved using different processing methods for 0% and 15% clay samples.

Soil sample ID (0% clay)	θ **[%]**	ε_{TDSP}	ε_{FWI}	ε_{SRM}	ε_{VMF}	**Soil sample ID (15% clay)**	θ **[%]**	ε_{TDSP}	ε_{FWI}	ε_{SRM}	ε_{VMF}
A1						*A1*					
Sample 1	0.00	2.53	2.65	3.46	3.12	Sample 28	0.00	3.97	4.02	3.89	4.01
Sample 2	2.68	3.64	3.50	3.02	3.55	Sample 29	8.42	4.32	3.98	3.56	5.36
Sample 3	4.44	5.34	5.30	3.86	3.83	Sample 30	18.27	5.67	5.35	5.41	6.93
Sample 4	4.26	6.42	6.49	4.28	3.80	Sample 31	21.69	6.00	5.68	6.88	7.48
Sample 5	5.11	8.46	8.50	3.53	3.94	Sample 32	23.95	8.63	8.78	8.89	7.84
Sample 6	5.73	10.43	10.52	3.76	4.03	Sample 33	27.11	9.04	8.82	11.52	8.35
Sample 7	6.71	12.9	13.22	4.62	4.19	Sample 34	29.44	12.21	12.28	11.13	8.72
Sample 8	8.34	15.96	16.20	2.63	4.45	Sample 35	31.76	12.30	12.37	13.11	9.09
Sample 9	12.18	20.09	20.59	27.74	5.07						
A2						*A2*					
Sample 10	0.00	2.74	2.78	2.21	3.33	Sample 36	0.00	4.07	4.06	4.05	4.03
Sample 11	3.62	3.96	3.73	2.94	3.91	Sample 37	9.71	3.91	3.75	3.86	5.58
Sample 12	6.06	4.60	4.52	3.00	4.30	Sample 38	17.99	4.36	4.41	3.02	6.91
Sample 13	7.27	5.93	5.55	3.70	4.50	Sample 39	20.96	4.72	4.80	4.07	7.38
Sample 14	10.48	8.79	8.44	3.56	5.01	Sample 40	24.89	5.47	5.58	4.79	8.01
Sample 15	14.71	11.07	10.69	3.36	5.69	Sample 41	27.13	6.00	5.91	6.28	8.37
Sample 16	21.43	14.44	14.02	3.41	6.76	Sample 42	30.29	6.75	7.16	8.39	8.88
Sample 17	24.68	17.79	17.91	4.47	7.28	Sample 43	33.20	6.85	7.35	9.05	9.34
Sample 18	29.44	21.10	20.60	11.46	8.05						
A3						*A3*					
Sample 19	0.00	2.64	2.66	2.44	3.26	Sample 44	0.00	3.43	3.38	2.76	3.68
Sample 20	2.80	3.22	3.04	2.28	3.71	Sample 45	9.69	4.02	4.03	4.21	5.23
Sample 21	5.55	3.96	3.80	3.24	4.15	Sample 46	15.46	3.38	3.37	3.01	6.15
Sample 22	8.07	4.84	4.66	3.13	4.55	Sample 47	18.10	3.69	3.65	3.08	6.57
Sample 23	10.95	5.87	5.52	4.45	5.01	Sample 48	21.08	4.02	3.88	3.92	7.05
Sample 24	13.61	6.14	5.69	3.97	5.44	Sample 49	23.79	4.18	4.07	4.17	7.48
Sample 25	17.42	8.06	7.83	4.61	6.05	Sample 50	26.00	4.42	4.69	4.03	7.84
Sample 26	20.87	11.54	11.27	5.67	6.60	Sample 51	29.40	4.65	4.84	4.44	8.38
Sample 27	26.63	15.19	14.91	7.07	7.52						

TABLE 2. Normalized Root Mean Square Deviation (NRMSD) values in clay-free soil samples by comparing the different permittivity-based methods.

Methods		**NRMSD**		
		A1	**A2**	**A3**
FWI	SRM	0.44	0.39	0.28
FWI	VMF	0.44	0.56	0.24
SRM	VMF	0.24	0.11	0.21
Topp Gen.	FWI	0.84	0.24	0.03
Topp Gen.	SRM	0.28	0.39	0.40
Topp Gen.	VMF	0.28	0.36	0.38
Topp SL	FWI	0.83	0.11	0.03
Topp SL	SRM	0.33	0.39	0.41
Topp SL	VMF	0.31	0.37	0.38

TABLE 3. Normalized Root Mean Square Deviation (NRMSD) values in clay-rich soil samples (15% of clay) by comparing the different permittivity-based methods.

Methods		**NMRSD**		
		A1	**A2**	**A3**
FWI	SRM	0.12	0.16	0.21
FWI	VMF	0.24	0.37	0.55
SRM	VMF	0.24	0.42	0.54
Topp Gen.	FWI	0.21	0.36	0.46
Topp Gen.	SRM	0.19	0.35	0.47
Topp Gen.	VMF	0.30	0.39	0.43

TABLE 4. Measured values of frequency spectra peaks f_P [Hz × 10^8] for 0% and 15% clay samples from dry to saturated conditions.

Soil sample ID (0% clay)	θ **[%]**	f_P **[Hz×10^8]**	**Soil sample ID (15% clay)**	θ **[%]**	f_P **[Hz×10^8]**
A1			*A1*		
Sample 1	0.00	6.65	Sample 28	0.00	5.68
Sample 2	2.68	5.87	Sample 29	8.42	5.51
Sample 3	4.44	5.48	Sample 30	18.27	5.29
Sample 4	4.26	5.28	Sample 31	21.69	5.09
Sample 5	5.11	4.50	Sample 32	23.95	2.54
Sample 6	5.73	4.70	Sample 33	27.11	2.54
Sample 7	6.71	2.54	Sample 34	29.44	2.35
Sample 8	8.34	2.54	Sample 35	31.76	2.35
Sample 9	12.18	2.15			
A2			*A2*		
Sample 10	0.00	6.46	Sample 36	0.00	5.87
Sample 11	3.62	5.87	Sample 37	9.71	5.87
Sample 12	6.06	5.28	Sample 38	17.99	5.68
Sample 13	7.27	5.09	Sample 39	20.96	5.48
Sample 14	10.48	5.09	Sample 40	24.89	5.28
Sample 15	14.71	4.70	Sample 41	27.13	5.28
Sample 16	21.43	2.54	Sample 42	30.29	5.87
Sample 17	24.68	2.34	Sample 43	33.20	5.68
Sample 18	29.44	2.15			
A3			*A3*		
Sample 19	0.00	6.65	Sample 44	0.00	6.07
Sample 20	2.80	6.26	Sample 45	9.69	5.68
Sample 21	5.55	5.87	Sample 46	15.46	5.87
Sample 22	8.07	5.28	Sample 47	18.10	5.87
Sample 23	10.95	5.09	Sample 48	21.08	5.87
Sample 24	13.61	5.87	Sample 49	23.79	5.69
Sample 25	17.42	5.28	Sample 50	26.00	5.67
Sample 26	20.87	5.28	Sample 51	29.40	4.50
Sample 27	26.63	4.50			

TABLE 5. Values of regression coefficients in Equation (18).

Clay Content [%]	**Parameter**	**Soil**		
		A1	**A2**	**A3**
0	$A \times 10^8$	6.79	6.43	6.64
	$B \times 10^7$	4.34	1.56	1.02
	R^2	0.84	0.95	0.77
15	$A \times 10^8$	6.34	5.83	5.96
	$B \times 10^7$	1.23	0.10	0.07
	R^2	0.71	0.98	0.99